Applied Energy 423 (2026) 128375

Contents lists available at ScienceDirect

Applied Energy

journal homepage: www.elsevier.com/locate/apen

Assessing scale-dependent aeroelastic load responses of 5 MW and 22 MW wind turbines under varying atmospheric stability

Nirav Dangi*, Jurij Sodja, Dominic von Terzi, Wei Yu

Delft University of Technology (TU Delft), Aerospace Engineering, Delft, 2629 HS, the Netherlands

HIGHLIGHTS

- Rotor-eddy interactions are investigated for a 5 MW and a 22 MW wind turbine.
- Novel use of wavelet coherence and cross power enables verification of findings in a physical manner.
- A new measurement-validated atmospheric-stability aware synthetic wind field framework is employed alongside IEC Kaimal wind field.
- For large turbines, IEC framework fails to model critical atmospheric structures, which are effectively addressed by the new framework.
- Effects of flexibility and reduced natural frequencies of the larger turbine, are shown to be secondary, in comparison to effects of rotor-eddy interactions.

ARTICLE INFO

Keywords:
Atmosphere
Wavelet
Coherence
Aeroelastic
Wind turbine
Rotor size

ABSTRACT

The upscaling of wind turbines has extended rotor-swept areas into the atmospheric boundary layer, several hundred meters above the surface layer. Traditional wind field models have relied on neutral surface-layer characteristics. Recent research emphasizes incorporating atmospheric stability and dynamics at higher altitudes, as larger turbines experience greater load variations due to eddies comparable in size to the rotor, causing non-uniform inflow.

This study evaluates a measurement-validated coherence model for aeroelastic analysis of a 5 MW and a 22 MW turbine. The model characterizes atmospheric stability using tuned coefficients and is applied alongside stability-dependent spectral wind field models. Six seeds of 30 minute simulations were conducted for each wind turbine model ranging from near cut-in to near cut-out wind speed, in intervals of 1 m/s, using on one hand, the proposed coherence model with stability-dependent spectra and on the other hand, the IEC Kaimal coherence model.

Aeroelastic results reveal distinct turbine responses to atmospheric stability. The trends of higher tower fore–aft bending moments in unstable conditions and lower moments in stable conditions, together with increased blade-root flapwise moments at above-rated wind speeds under stable, high-shear conditions, are captured.

Wavelet analysis confirms that larger turbines face greater load variations because eddies are smaller than the rotor, whereas smaller turbines experience more uniform frequency-time correlations with hub-height velocity. Simulations with flexible and rigid blades and towers indicate that flexibility effects are secondary to eddy size and coherence. Overall, it is demonstrated that simple stability-dependent empirical coherence and spectral models can effectively replicate the commonly observed impact of atmospheric stability on wind turbine loads.

1. Introduction

Since the early 2000s, the expansion of installed wind power capacity has been accompanied by a pronounced shift toward larger wind turbine designs, characterised by higher hub heights and longer blades, to leverage economies of scale. The enlargement of rotor diameters enables turbines to sweep larger areas, experience higher wind speeds, capture more kinetic energy, and consequently generate more 5electricity. Between 2001 and 2021, the median rotor diameter increased by 104%, from 76 m to 155 m, while the median rated power (PR) rose by 175%, from 2 MW to 5.5 MW [1,2]. By 2024, offshore wind turbines connected to the grid exhibited an average rated power of 10.1 MW, with the

* Corresponding author.
Email address: N.S.Dangi@tudelft.nl (N. Dangi).

https://doi.org/10.1016/j.apenergy.2026.128375
Received 11 April 2026; Received in revised form 11 June 2026; Accepted 4 July 2026
Available online 11 July 2026

largest installed units—rated at 14.7 MW and featuring a 222 m rotor diameter—operating at the Moray West offshore wind farm [3]. In contrast, the average rated power of offshore turbines commissioned in 2014 was 4.2 MW [3].

The continued upscaling of wind turbines necessitates a critical reassessment of existing design certification requirements and the representation of atmospheric inflows encountered by these larger machines. The current wind turbine design standard established by the International Electrotechnical Commission (IEC) [4,5] prescribes two main spectral approaches for simulating wind fields: the semi-physical Mann model [7,8] and the Kaimal model, which employs a modified form of Kaimal autospectrum [9] in conjunction with a modified version [10] of Davenport's exponential coherence formulation [11]. Both models were originally developed for the atmospheric surface layer and, as such, do not fully capture the complex flow dynamics present within the atmospheric boundary layer at higher altitudes. Moreover, they assume neutral atmospheric stability, whereas offshore environments are frequently characterised by non-neutral stratification [12–14]. It should be noted that the original Kaimal spectrum did involve a dependence on measurement height (z), wind speed, and atmospheric stability, by means of $z/L_{M\text{-}O}$, where $L_{M\text{-}O}$ is the Monin-Obukhov length [15–17]. The $L_{M\text{-}O}$ is generally connected to a dimensional analysis of the equation of turbulent kinetic energy and the ratio of the buoyancy and shearing effects [18–20]. Several other spectral models are available in the literature. Some of these spectral models were studied, evaluated, and enhanced in [21,22].

Currently, the IEC design standards do not explicitly account for non-neutral atmospheric conditions in wind turbine load assessments. In practice, the Mann model parameters are often tuned to site-specific atmospheric spectra [4] to represent various stability regimes, despite the model being formulated under neutral conditions. Conversely, the IEC guidelines prescribe the IEC-Kaimal model with a spectrum and coherence model defined strictly for neutral stability.

The study in [12] presents a comparative analysis of velocity spectra and vertical coherence estimates in the marine ABL. Their study utilises measurements recorded up to 81.5 m. A part of their study compares the measured velocity spectra with existing spectral models and provides a table of fitted parameters for the models. These parameters were provided extensively as functions of both measured altitude and stability. Furthermore, the two-parameter IEC coherence model was fitted to the vertical coherence estimates, and the parameters were found to be exponential functions of atmospheric stability. However, they find the fit to be reliable only for ranges of $-2 < z/L_{M\text{-}O} < 0.2$, whereas the stability bins were defined between $-2 < z/L_{M\text{-}O} < 2$. This suggests the need for further investigation of the positive regime encompassing near-neutral-stable to very stable conditions, in addition to assessing the fit parameters for higher altitude wind measurements. It is also worth noting that the impact of the coherence and spectral model parameters obtained was not investigated; therefore, it remains unclear what effect these updated parameters have on wind loads.

Existing literature has shown the non-negligible impact of atmospheric stability on wind turbine loads. Two of the earliest detailed aeroelastic studies focusing on the impact of atmospheric stability on wind turbine loads can be considered as [23,24]. In [24], the authors report the impact of different wind shear and turbulence in differently stratified wind fields on the rotor and tower blades. They provide intuitive insights about the expected impact of larger eddies in the flow. This reasoning enables a widespread understanding that, as the rotor diameter increases, the largest eddies in the flow lead to greater non-uniformity across the rotor, whereas they may appear uniform to a smaller rotor. Nevertheless, a detailed physical explanation or validation of these interactions, especially across wind turbines of different sizes, is not yet available, and many studies have reported only the final impact on loads. In [25,26], the atmospheric stability impact on a floating wind turbine was studied. In [27], the study involved assessing the impact of atmospheric stability on the loads of a 6 MW spar-type floating wind turbine. They compared simulation results with observations and found that load differences across atmospheric conditions were more pronounced in observations than in simulations. They attribute this, in part, to the lateral coherence modelling. Recently, in [28], the authors used Spectral Proper Orthogonal Decomposition (SPOD) to understand the impact of coherent structures in different ABLs, on a 22 MW wind turbine's loads. The differences between coherence from high-fidelity simulations and that from the IEC Kaimal model were highlighted. However, the extension of the IEC Kaimal model was left for future work.

More recently, also focusing on large wind turbines, the authors in [29] assess the impact of turbulence inhomogeneity on a 22 MW wind turbine. They do this by modifying the coherence of the Mann model using a weighted average of coherence in the standard homogeneous wind fields. They report a non-negligible impact on tower loads under inhomogeneous wind fields. However, this methodological assumption was only a choice and was noted as a limitation by the authors. They recommended validating this approach with site-specific coherence estimates and the resulting aeroelastic impact. Moreover, in their study, the Østerild test site data were used, which is an onshore site. In [30], the Syed-Mann model [31] was used with FINO1 site data, which has measurements only up to 100 m altitude. Lastly, a recent study [32], relevant to large wind turbines, utilised load measurements from a 15 MW wind turbine and compared them with loads obtained from simulations using the Mann model with site-specific parameters. They conclude that overall agreement is good, with differences between measurements and simulations of around 3 standard deviations, but they note differences of up to 11 standard deviations in key wind-speed regions and in non-neutral atmospheres. They attribute these differences to incorrect estimates of vertical coherence from the model and wind shear assimilation. The lateral coherence, more relevant for aeroelastic predictions, was not measured in the study; hence, some differences remained unexplained. This recent literature indicates that no study has utilised coherence estimates from measurements at altitudes up to 300 m for the aeroelastic assessment of large wind turbines.

Motivated by these gaps, the authors recently proposed a new, measurement-validated, atmospheric-stability-dependent empirical coherence model in [33]. This model was tested on measurements [34,35] at high altitudes upto 287 m and lateral separations upto 241 m. This framework coupled with the use of stability-varying empirical spectral formulations [21,22] enables generating wind fields with improved physical realism while maintaining computational efficiency. In contrast, although the Mann model offers greater physical fidelity, it requires parameter fitting and computationally intensive field-generation procedures—still far less demanding than large-eddy simulations (LES) of the atmospheric boundary layer but more than empirical spectral approaches for grid cells lower than 64×64. While numerous studies have explored the performance of the Mann model at different sites, comparatively little to no research has focused on developing and evaluating a new formulation with the same framework and computational ease as the Kaimal-based approach, to account for stability effects. It can also be noted that the IEC 61400-13 standard for load verification [6] does not account for variations in turbulence spectral models and advises only the freestream wind profile and turbulence intensity. This leads to the IEC Kaimal model being the preferred choice due to its simplicity [29]. Therefore, the proposed semi-empirical framework in this study provides a crucial, simplified approach for engineering load simulations at the design stage.

This study addresses the aforementioned research gaps by evaluating the stability-dependent empirical coherence model proposed by the authors [33] for aeroelastic simulations. The coherence model is applied in conjunction with existing stability-dependent spectral models. Simulations are performed across the operational range, from near cut-in to near cut-out wind speeds, for both the NREL 5 MW [36] and the IEA 22 MW wind turbine [37], in representative neutral, stable, and unstable synthetic inflow wind fields. Accordingly, the study addresses the following research questions: (1) What are the aeroelastic load trends when an empirical stability-dependent coherence model and spectra are employed? (2) How and why does the impact of this model differ between a smaller (5 MW) and a larger (22 MW) wind turbine?

2. Methods

The study primarily employs three methods: first, inflow turbulence generation; second, aeroelastic load simulation and analysis; and third, wavelet analysis. Each method is described in detail in the following sections.

2.1. Inflow turbulence generation

Inflow turbulence can be generated using various methods (see [38]). In line with IEC standards, this study employs synthetic wind field generation based on Fourier techniques. The focus is on improving the straightforward methodology, as in the IEC-Kaimal model with the IEC-Kaimal spectrum.

Fourier techniques for generating inflow turbulence are based on synthesising turbulence as a set of harmonic functions using Fourier analysis. Typically, the procedure involves using Fourier modes with random phases and a target wind-field energy spectrum to generate spatially uncorrelated wind-field fluctuations. Next, a coherence function is introduced, and the spatial correlation information is added using Cholesky decomposition [39]. Lastly, the desired mean wind profile is added to the fluctuations, resulting in a temporally (using target spectra) and spatially (using target coherence function) correlated wind field, albeit with random phases. The details of the former are given in Section 2.1.1 and the latter is explained along with the proposed coherence model in Section 2.1.2.

2.1.1. Spectral models

The IEC standard specifies the use of the IEC-Kaimal spectrum along with the Kaimal coherence function. The IEC-Kaimal spectrum, as noted previously, is intended for neutral atmospheric conditions. The Kaimal spectrum is given by Eq. (1).

$$\frac{f S_k(f)}{\sigma_k^2} = \frac{4 f L_K / V_{hub}}{(1 + 6 f L_K / V_{hub})^{5/3}} \tag{1}$$

In Eq. (1), f is the frequency in Hertz (Hz), S_k is the spectrum of the k^{th} velocity component, where $k \in (1,2,3)$, for the u, v, and the w component respectively. The stream-wise velocity at hub-height (z_{hub}) is given by V_{hub}. Next, the IEC standard specifies a parameter resembling a length scale, L_K, not to be confused with the turbulence integral length scale (denoted later as $\mathcal{L}$). This parameter is further dependent on a scale parameter Λ as shown in Eq. (2).

$$\begin{aligned} \Lambda &= \min(0.7 z_{\text{hub}}, 42), \\ L_u &= 8.1\,\Lambda, \\ L_v &= 2.7\,\Lambda, \\ L_w &= 0.66\,\Lambda. \end{aligned} \tag{2}$$

Lastly, the σ_K parameter controls the desired standard deviation of the corresponding velocity component. Upon choosing the σ_u, Eq. (3) is used in accordance with the IEC standards.

$$\begin{aligned} \sigma_v &= 0.8\sigma_u, \\ \sigma_w &= 0.5\sigma_u \end{aligned} \tag{3}$$

A few comments can be made on the formulation of the IEC-Kaimal spectrum shown in Eq. (1). Firstly, a dependence of the spectrum on altitude is absent, excluding the scaling differences obtained for altitudes below and above 42 m using the parameter Λ (Eq. 2). Furthermore, the formulation does not explicitly distinguish between atmospheric stabilities. An implicit dependence can be achieved if one modifies the σ_k parameter for different atmospheric stabilities. However, it becomes clear that this approach will not allow for a change in the energy distribution across frequencies, which would resemble stratification. These limitations do not allow for capturing non-neutral conditions using Eq. (1). Hence, it is worthwhile to investigate the impact of using stability-dependent spectral models in comparison to the IEC-Kaimal formulation.

As mentioned previously, out of the several existing spectral models, this study utilises the models from [21,22]. These spectral models are also part of the open-source code NREL `TurbSim` [40] and can be used by the user upon choosing the Risø `SMOOTH` terrain model. The formulations for the neutral and stable atmospheric stratification are shown in Eqs. (4) to (6), separately for the u, v, and the w components, respectively.

$$\frac{f S_u}{u_{*,0}^2} = \frac{79(f_r/q)}{1 + 263(f_r/q)^{5/3}} \left(\frac{\phi_e}{q}\right)^{2/3} \tag{4}$$

$$\frac{f S_v}{u_{*,0}^2} = \frac{13(f_r/q)}{1 + 32(f_r/q)^{5/3}} \left(\frac{\phi_e}{q}\right)^{2/3} \tag{5}$$

$$\frac{f S_w}{u_{*,0}^2} = \frac{3.5(f_r/q)}{1 + 8.6(f_r/q)^{5/3}} \left(\frac{\phi_e}{q}\right)^{2/3} \tag{6}$$

The parameter f_r is the reduced frequency which is given by $f_r = fz/U \in (u, v, w)$. The surface friction velocity, $u_{*,0}$, is used to scale the spectrum, unlike the σ_K scaling in Eq. (1). Lastly, the atmospheric stability dependence is achieved by inputting the parameters ϕ_e and q, which depend on the altitude and $L_{M\text{-}O}$, as shown in Eqs. (7) and (8), respectively.

$$\phi_e^{2/3} = 1 + 2.5(z/L_{M-O})^{0.6}, \quad 0 < z/L_{M-O} < 2 \tag{7}$$

$$q = \phi_m = 1 + 4.7 z/L_{M-O} \tag{8}$$

In Eq. (7), ϕ_e is a dimensional turbulence energy dissipation rate, as defined in [9]. In Eq. (8), ϕ_m is the dimensionless velocity gradient, and the factor q is connected to it as in [41]. As evident from the above formulations, one needs to choose a suitable $L_{M\text{-}O}$. In this study, the atmospheric stability and $L_{M\text{-}O}$ are chosen as per [42]. For a stable atmosphere, $L_{M\text{-}O} = 350$ is used and $L_{M\text{-}O} = 10^{10}$ is used for the neutral atmosphere. Next, the unstable atmosphere spectral formulations are given in Eqs. (9) to (11), separately for the u, v, and the w components, respectively.

$$\frac{f S_u}{u_{*,0}^2} = \frac{0.5 f_i}{1 + 2.2 f_i^{5/3}} \left(\frac{z_i}{-L_{M-O}}\right)^{2/3} + \frac{105 f_{rru}}{(1 + 33 f_{rru})^{5/3}} \frac{(1 - z/z_i)^2}{(1 + 15 z/z_i)^{2/3}} \tag{9}$$

$$\frac{f S_v}{u_{*,0}^2} = \frac{0.95 f_i}{1 + 2 f_i^{5/3}} \left(\frac{z_i}{-L_{M-O}}\right)^{2/3} + \frac{17 f_{rrv}}{(1 + 9.5 f_{rrv})^{5/3}} \frac{(1 - z/z_i)^2}{(1 + 2.8 z/z_i)^{2/3}} \tag{10}$$

$$\frac{f S_w}{u_{*,0}^2} = F(f_r, z/z_i) \frac{0.95 f_i}{1 + 2 f_i^{5/3}} \left(\frac{z_i}{-L}\right)^{2/3} + \frac{2 f_r}{(1 + 5.3 f_r)^{5/3}} (1 - z/z_i)^2 \tag{11}$$

In the equations above for the unstable atmosphere spectrum, one may note that these comprise two terms. The spectral formulation is given as a sum of spectra for the low- and high-wavenumber regions. Two additional dimensionless frequencies are introduced for the u and the v component given as f_{rru}, and f_{rrv}, respectively, in Eq. (12). Additionally a filter function, $F(f_r, z/z_i)$ is prescribed for the w component.

$$\begin{aligned} f_{rru} &= \frac{f_r}{1 + 15 z/z_i} \\ f_{rrv} &= \frac{f_r}{1 + 2.8 z/z_i} \\ F(f_r, z/z_i) &= \left[\frac{f_r^2 + (0.3 z/z_i)^2}{f_r^2 + 0.15^2}\right]^{1/2} \end{aligned} \tag{12}$$

In these spectral formulations, the parameter z_i is introduced, typically referred to as the boundary layer height or the inversion layer height. Additionally, a dimensionless frequency in relation to this height is denoted by $f_i = \frac{f z_i}{U \in (u,v,w)}$. From above formulations, it is evident that one should choose appropriate values for the z_i and $L_{M\text{-}O}$ resembling an unstable atmosphere. Once again, as per [42], $L_{M\text{-}O} = -350$ is chosen and $z_i = 2000$ m is chosen.

A few comments can be made about the extensive spectral formulations listed for the neutral, stable, and unstable stratification. Firstly, it is clear that a dependence on atmospheric stability is accounted for, which enhances the wind field. Secondly, the friction-velocity scaling is achieved for the spectrum, which may be more realistic than the implicit turbulence scaling. Thus, one should note that using the equations from [21,22], the σ_K, the standard deviation of the different velocity components, is obtained after wind field generation, and one should then apply a uniform scaling factor based on the desired standard deviation. The chosen standard deviation is discussed later in Section 3. Thirdly, the atmospheric inhomogeneity arises because the spectral formulations depend on altitude. Lastly, it should be noted that, due to a lack of high-quality measurements at higher altitudes, this spectral formulation is intended only for the lower part of the atmospheric boundary layer. In [40], it is noted to be applicable up to 120 m, which still does not encompass all the altitudes swept by the larger wind turbines.

2.1.2. Coherence models

The synthetic wind field generation by Fourier methods involves the use of coherence function(s) to add spatial coherence to the wind field. A mathematical coherence formulation was used to assess the coherence of the obtained wind field. The co-coherence, quad-coherence, and root-coherence were computed (Eq. (13), where f is the frequency). These refer to the real part, imaginary part, and amplitude of a two-point cross-spectrum, respectively, normalised by the product of power spectra for each point [43].

$$\gamma = \underbrace{\frac{\mathrm{Re}\left[S_{xy}(f)\right]}{\sqrt{S_{xx}(f)S_{yy}(f)}}}_{\text{co-coherence}} + \underbrace{\frac{\mathrm{Im}\left[S_{xy}(f)\right]}{\sqrt{S_{xx}(f)S_{yy}(f)}}}_{\text{quad-coherence}} \tag{13}$$

The magnitude-squared coherence as shown in Eq. (14) will be presented and discussed later in this study, mainly because the quad-coherence is known to have a negligible influence on aeroelastic loads [44].

$$\gamma^2 = \frac{|S_{xy(f)}|^2}{(S_{xx}(f)S_{yy}(f))} \tag{14}$$

All estimates of γ^2 are later provided using the Welch method [45] with 7 segments, 50% overlap, and a Hann window function. A simple moving average filter over 5 points smoothed the resulting co-coherence estimates.

The IEC coherence (γ^2_{IEC}) function for an arbitrary separation r is given in Eq. (15) [4,46].

$$\gamma^2_{\mathrm{IEC}}(r,f) = \left(\exp\left(-12\sqrt{\left(\frac{f\cdot r}{V_{\mathrm{hub}}}\right)^2 + \left(\frac{0.12\cdot r}{L_{c,\mathrm{IEC}}}\right)^2}\right)\right)^2 \tag{15}$$

where f is the frequency in Hz, r represents the length of the projection of the vector that separates the two points onto a plane that is perpendicular to the average direction of the wind, L_c is the coherence scale parameter as defined for the u component in Eq. (2), and V_{hub} is the stream-wise velocity at the hub height. Three drawbacks of this formulation were addressed while developing a new empirical coherence model, which will be discussed below. Firstly, it can be noted that in Eq. (15), there is no distinction between atmospheric stability. Secondly, the model does not allow for anisotropy because the formulation is meant to be applied for any arbitrary separation r rather than using different model parameters for different directions. Thirdly, the formulation does not differentiate between coherence for different velocity components. This is because the formulation is originally intended only for the u component, and its use for other components is not specified.

Table 1
Proposed lateral coherence model fit parameters for the u and v components. The acronyms “NABL”, “SABL”, “USABL” stand for neutral, stable, and unstable ABL.

Atmospheric stability	a_y		β_y	
	u comp.	v comp.	u comp.	v comp.
NABL	35	9	1.16	1.00
SABL	8	8	0.81	0.88
USABL	39	11	1.36	1.24

Hence, the aim was to address these drawbacks while remaining inspired by the IEC formulation for its ease and flexibility. Another source of inspiration was the Shiotani-Iwatani coherence function [47]. The proposed coherence model was developed, calibrated, and compared against measurements from [34,35], as detailed in [33]. The proposed coherence function(s) are shown in Eq. (16) and the final interpolated coherence function is shown in Eq. (17) (Table 1).

$$\gamma_z^2 = \exp\left[-a_z\left(\left(f\frac{\Delta z}{V}\right)^{\beta_z} + \left(0.05\frac{\Delta z}{L_{c,\mathrm{IEC}}}\right)^{\beta_z}\right)\right], \quad \gamma_y^2 = \exp\left[-a_y\left(\left(f\frac{\Delta y}{V}\right)^{\beta_y} + \left(0.05\frac{\Delta y}{L_{c,\mathrm{IEC}}}\right)^{\beta_y}\right)\right] \tag{16}$$

$$\gamma_{yz}^2 = \exp\left[-\sqrt{\left[a_y((f\frac{\Delta y}{V})^{\beta_y} + (0.05\frac{\Delta y}{L_{c,\mathrm{IEC}}})^{\beta_y})\right]^2 + \ldots + \left[a_z((f\frac{\Delta z}{V})^{\beta_z} + (0.05\frac{\Delta z}{L_{c,\mathrm{IEC}}})^{\beta_z})\right]^2}\right] \tag{17}$$

2.2. Wavelet transform and coherence

Wavelet analysis enables the decomposition of a time series into a time-frequency space. Thus, one can determine both the dominant modes of variability and how those modes vary in time [48]. Wavelet analysis offers time–frequency localisation, capturing transient or non-stationary features that Fourier analysis smooths over. The classical version of the Heisenberg uncertainty principle implies that there is always a trade-off between localisation in time and frequency [49]. Fourier analysis provides a global frequency decomposition that is ideal for stationary, periodic signals, but lacks temporal information. Wavelets thus enable adaptive, multi-scale representations, whereas Fourier methods give fixed-resolution spectral information. Wavelet analysis has been found to be a powerful tool in several fields, such as finance [50,51], geophysics [49,52], and more specifically for atmospheric influence on wind turbine loads [53,54].

For a general background on wavelets and wavelet transforms, the reader is referred to [48,49]. In this study, wavelet coherence and wavelet cross power are employed to enable a more detailed analysis of the results. Given the quasi-stationary nature of the wind fields considered here—i.e., lacking significant non-stationarity—replacing Fourier analysis entirely with wavelet analysis would not provide substantial additional benefit. However, substituting spectral coherence (Eq. 13) with wavelet coherence provides significantly greater insight, as it captures cross-correlation between two signals in both time and frequency domains, rather than solely in frequency space as in Fourier analysis. It can also be noted that the standard frequency-domain analysis of wind turbine loads is well established in the existing literature- for instance, the

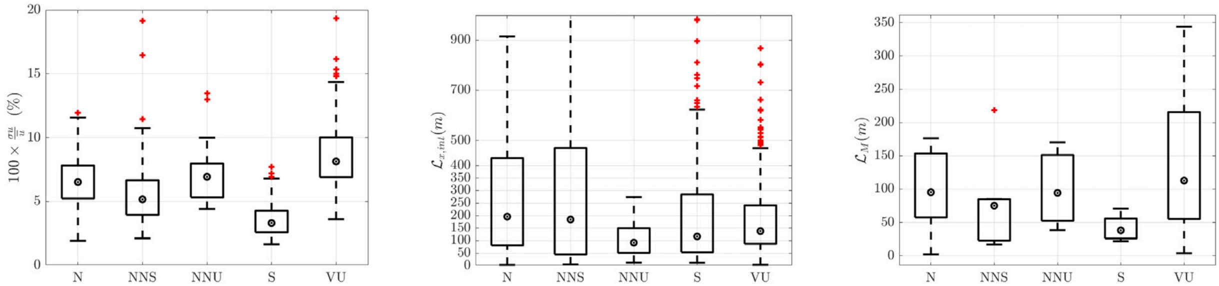

(a) Stream-wise component turbulence intensity (TI) in percentage.
(b) Stream-wise component integral length scale.
(c) Mann model length scale.

Fig. 1. Key physical parameters after post-processing the LiDAR measurements. The parameters are shown in box-and-whisker plots at different atmospheric stabilities. N stands for neutral, S stands for stable, U stands for unstable, prefix NN stands for near neutral, and prefix V stands for very. Boxes show the median and interquartile range; whiskers show non-outlier extremes, and outliers are marked with '+'.

importance of low frequency coherence on aeroelastic loads [28,44,55]. Hence, to gain more unique insights into the aeroelastic phenomenon, wavelet analysis has been used in the present study.

With the estimation of the continuous wavelet transform (CWT) at hand, one can obtain the cross wavelet transform (XWT) between two signals, x, and y, as $\mathcal{W}^{xy} = \mathcal{W}^x \mathcal{W}^{y*}$. The cross-wavelet power can be evaluated as $|\mathcal{W}^{xy}|$, which reveals regions of high common power. Similar to Eq. (14), one can obtain the wavelet coherence by replacing the Fourier transform with the wavelet transform- in practice, a smoothing operator is also utilised, for which the reader is referred to [48]. In this study, the `MATLAB` functions `cwt` and `wcoherence` were used for the results.

Wavelet coherence was applied to velocity signals and wind turbine load measurements, enabling the identification of when and how often these quantities are correlated. Additionally, wavelet cross power is evaluated to identify regions of amplified shared power between the signals.

3. Simulation setup

This study employs the spectral wind field generation method developed by Shinozuka and Deodatis [56] and incorporates necessary modifications to the open-source `MATLAB` code from [57] to facilitate the desired coherence and spectral formulations. This open-source code [57] was originally used in [58] and demonstrated computational efficiency, as noted in [59]. It was also recently used and validated in [60]. It can also be noted that for wind energy applications, spectral wind fields were first presented and applied by Veers [61].

Both, the reference NREL 5 MW wind turbine (rated wind speed of 11.4 m/s) [36] and the larger offshore reference IEA 22 MW wind turbine (rated wind speed of 11 m/s) [37] were used to demonstrate the capabilities and the impact of the coherence model on two vastly different wind turbines, both, in terms of flexibility (for instance, due to the increased blade flexibiility, and lower natural frequencies for the larger wind turbine) and size. The NREL 5 MW wind turbine operates at a rated rotor speed of 12.1 RPM, whereas the IEA 22 MW wind turbine operates at 7.06 RPM. This rated rotor speed corresponds to a 1 P frequency of 0.2 Hz, and 0.12 Hz respectively. The approximate minimum rotor speed during the simulations was 9 RPM for the NREL 5 MW wind turbine and 3 RPM for the IEA 22 MW wind turbine. This implies a rough range of turbine rotational frequency as $0.15 < P_{5MW} < 0.2$ Hz, and $0.05 < P_{22MW} < 0.12$ Hz.

The range of hub-height wind speeds chosen were 6.5 m/s to 20.5 m/s in steps of 1 m/s. Operational regions very close to the cut-in and cut-out wind speeds ($u_{\infty,\text{hub}} \leq 5.5$m/s and $u_{\infty,\text{hub}} \geq 21.5$m/s) were excluded because these regions showed large aeroelastic load standard deviations across seeds. A total of 6 seeds were used at each wind speed. The simulation time of each seed was 2048 s of which the first 248 s were discarded as initial transients. This leads to a 30 minute simulation period for each seed (note that the IEC recommends a 10 minute simulation period for each seed). The spectral formulations and coherence models discussed in Section 2 were utilised. Synthetic wind fields resembling neutral, stable, and unstable atmospheres were simulated alongside the IEC-Kaimal coherence model-based wind field. Hence, a total of $2 \times 15 \times 6 \times 4 = 720$ simulations were run and analysed. Having noted the differences in the IEC-Kaimal spectrum (Eq. 1), and the neutral atmosphere spectrum (Eqs. (4) to (6)), the IEC-Kaimal coherence model was used with the neutral atmosphere spectrum, to avoid differences in aeroelastic response due to energy spectrum.

As mentioned previously, a choice of the desired mean wind profile must be made. The mean wind profiles were chosen as wind fields varying with altitude according to the power-law formula as shown in Eq. (18), where α is the wind shear exponent.

$$U(z) = U(z_{\text{hub}})\left(z/z_{\text{hub}}\right)^{\alpha} \tag{18}$$

Here, the neutral atmosphere was modelled as a wind field with $\alpha = 0.2$, a stable atmosphere with $\alpha = 0.25$, and an unstable atmosphere with $\alpha = 0.1$. It can be noted that the use of power law wind shear was made in line with the IEC guidelines [5] and neglects the Monin-Obukhov similarity theory (MOST) based wind shear. However, for the purposes of this study, either method could be used without affecting the final conclusions, as the key aspect to be captured was wind shear, alongside accurate coherence and energy spectra for different boundary layers.

Additionally, to ensure representative turbulence intensities across the different stratifications, the desired turbulence intensity must be selected. For this purpose, the measurements from [34,35], which were also used for the tuning of the proposed coherence model, were processed, and some key parameters were extracted, as shown in Fig. 1. The reader is referred to [35] for details on the measurement setup.

Firstly, the turbulence intensity (TI) during the measurement periods was assessed as shown in Fig. 1(a). The TI was calculated as $100 \times \sigma_u/\bar{u}$, where the time-average of the stream-wise component $\bar{u}$ and the standard deviation of the stream-wise component σ_u, were calculated over the available 20 minute time duration. It can be noted that for a stable (S) atmosphere, the median TI is approximately 4 %, while for a neutral (N) and an unstable (US) atmosphere, the median TI is approximately similar at 8 %. These were the values utilised for the desired hub-height turbulence intensity in the synthetic wind fields. Next, the stream-wise turbulence integral length scales $\mathcal{L}_{x,\text{int}}$ were calculated with the formulations described in [62] and shown in Eq. (19).

$$\begin{aligned} \mathcal{L}_x &= \bar{u} \cdot \int_{t=0}^{t(R_i(t)=0)} R_i(t)\mathrm{d}t \\ \mathcal{L}_y &= \int_0^{+\infty} R_i(\Delta_y), \mathrm{d}\Delta_y \end{aligned} \tag{19}$$

Table 2
Atmospheric-stability–dependent coherence model simulation setup.

Parameter	NABL	SABL	USABL	IEC
Wind Turbines	NREL 5 MW, and IEA 22 MW			
$u_{\infty,hub}$	6.5–20.5 m/s (1 m/s step, 15 cases)			
Random Seeds	6			
Energy Spectrum	Atmospoheric-stability-dependent spectral models			
Coherence Model	Proposed coherence model			IEC–Kaimal
Mean Wind Shear (α_{pow})	0.2	0.25	0.1	0.2
Hub-Height TI	8%	4%	8%	8%
Wind Fields per Class	15 wind speeds × 6 seeds = 90			
Total Wind Fields	2 wind turbines × 4 coherence models × 90 = 720			
Simulation Time	2048 s per seed; first 248 s discarded (30 min usable)			

In Eq. (19), R_i is the single-sided auto-covariance function of the fluctuating wind velocity, that is, the de-trended velocity signal. $\mathcal{L}_x$ was computed on the basis of the integration up to the first zero-crossing [63] of R_i. The $\mathcal{L}_y$ was computed by an integral of an exponential decay function to approximate the correlation coefficients as a function of span-wise separation [62]. The results of $\mathcal{L}_x$ are shown in Fig. 1(b). One can think of the turbulence integral length scale as the size of the eddies containing the highest energy.

The values of $\mathcal{L}_x$ in Fig. 1(b) indicate the expectation that the stable atmosphere has the lowest integral length scales due to, for instance, the lack of active turbulence mixing. Once again, owing to the similar turbulence, the neutral and unstable atmospheres are seen to feature similar median integral length scales. However, the more outliers in the unstable case are once again evident. The cause of the outliers in the stable atmosphere remains unclear. This might be due to lower sampling frequencies than desired for more accurate estimation of such quantities, or to the measurement equipment (in the case of [34,35], LiDARs).

Finally, to reduce noise in the observed parameters, a systematic parameter-fitting procedure was applied to the velocity spectrum using the Mann model. The fit parameters were also provided by the authors of [34,35], of which, the $\mathcal{L}_M$ is hereby reported, in Fig. 1(c). It is now clearer that the stream-wise integral length scales in the stable atmosphere are about half of those in the neutral and unstable atmosphere. The higher range of length scales in the unstable atmosphere is also clarified. These trends in length scales will aid in demonstrating the realism of the generated synthetic wind fields and their corresponding aeroelastic impact. A final summary of the simulation setup is provided in Table 2.

3.1. Inflow profiles

The wind shear, the turbulence shear, and the integral length scales of the stream-wise component in the generated wind fields are shown in the respective figures of Fig. 2. From this point onwards, the IEC nomenclature is used for the IEC-Kaimal coherence model-based wind field, and NABL, SABL, and USABL are used for neutral, stable, and unstable atmospheric wind fields, with the above-discussed inputs and the coherence and spectral formulations and parameters described earlier. The wind shear normalised by the hub-height stream-wise velocity, shown in Fig. 2(a) was used for the near cut-in to near cut-out wind speed simulations. The planar-averaged turbulence shear is shown in Fig. 2(b). It may be noted that the wind shear exponent values chosen are only a few representative values that the wind turbine will be exposed to. One may consider it worthwhile to conduct a sensitivity analysis on the aeroelastic impact; however, this is not the scope of this study. The reader is referred to [64] for insights into this matter. As mentioned previously, the desired hub-height TI for the stream-wise component was 8 % for the neutral and unstable atmosphere, while 4 % for the stable atmospheric wind fields, based on the previously discussed measurements. The higher TI in the unstable atmosphere compared to the neutral atmosphere is evident and may have some relevance to the aeroelastic impact to a certain extent. This difference was inherent in the spectral formulations used alongside the coherence functions. One should thus scale the resulting wind-field TI only with respect to a target point, here, the hub-height. Scaling each point to the desired value destroys spatial coherence; thus, it is not applied here. In summary, it can be noted that the presented and utilised turbulence intensity (TI) variation against altitude is a (uniformly scaled) output of the model, not an input to the model. The model is constrained by a target TI at hub height; a global scaling factor (as also recommended by the IEC guidelines [5]) is derived from the ratio of this target value to the unscaled model output at the same elevation. This factor is then applied uniformly across the altitude range, ensuring the profile is anchored to the desired hub-height conditions while preserving the model's predicted vertical gradient.

Lastly, Fig. 2(c) shows the span-wise integral length scales ($\mathcal{L}_u^y$) in the wind field. It is observed that the USABL wind field features the highest integral length scales, followed by NABL and the SABL wind fields. These trends are in line with the remarks discussed by means of Fig. 1. The IEC wind field generally has integral length scales similar to or lower than those of both the NABL and SABL wind fields.

3.2. Spectral features

The higher-order statistics of the wind field are briefly discussed here to highlight differences among various atmospheric wind fields. Firstly, the frequency-multiplied energy spectra of the different wind speed components at the hub-height of the NREL 5 MW wind turbine are shown in Fig. 3. It is evident that the energy distribution in the unstable and stable atmosphere spectra is notably different from the neutral atmosphere spectrum. It is also noted once again that the choice was made to use the neutral atmosphere spectra in the IEC-Kaimal coherence model-based wind fields; thus, the minor differences in spectral content of the IEC and NABL wind fields in Fig. 3, are primarily due to numerical factors.

Due to the lower turbulence in stable atmospheric wind fields, the stable atmosphere spectrum has approximately half the energy at all frequencies for all velocity components. The unstable atmosphere features higher energy than the neutral atmosphere at frequencies greater than 10^{-2} Hz. However, it is worth noting that these features may vary slightly with the altitude analysed and with different inputs of $L_{M\text{-}O}$ and z_i, among other factors. With this discussion, one can thus appreciate the differences in energy spectra between the atmospheres, which will inherently lead to different wind turbine aeroelastic responses.

Next, the coherence in the wind field is assessed. The estimates from the generated wind fields are presented, where it may be recalled that the proposed coherence model was validated in an earlier study [28] with measurements. In Fig. 4, the coherence is presented for the stream-wise component. This visualisation serves as validation of the implementation of synthetic wind field generation and helps illustrate differences in the atmosphere that are not captured by the current simplistic IEC Kaimal coherence formulation and parameters. The γ^2_{uu} for measurement points laterally separated by a separation distance of 20 m is assessed for in Fig. 4(a) and for a lateral separation of 60 m in Fig. 4(b). The four subplots show the values at different altitudes, ranging from 55 m to 175 m. As expected, the coherence decreases with increasing separation distance. Among the different atmospheres, the unstable atmosphere has the highest coherence, along with the highest integral length scales, and coherence generally decreases from unstable to neutral to stable. This is also consistent with existing literature, for example, [12,27,28,44,65]. The IEC-Kaimal coherence function generally shows the least coherence at frequencies below 0.01 Hz. Similarly, it can be noted that the use of the proposed coherence formulation and parameters, as intended, yields different coherence values, especially at lower frequencies below 0.1 Hz, while it performs similarly to the IEC-Kaimal coherence function otherwise. Next, for the cross-stream component, the γ^2_{vv} is shown in Fig. 5, for measurement points laterally separated by 20 m and 60 m, in Fig. 5(a) and (b), respectively. The cross-stream component coherence is seen to be higher than the stream-wise component, given the lateral separation being assessed. Larger differences

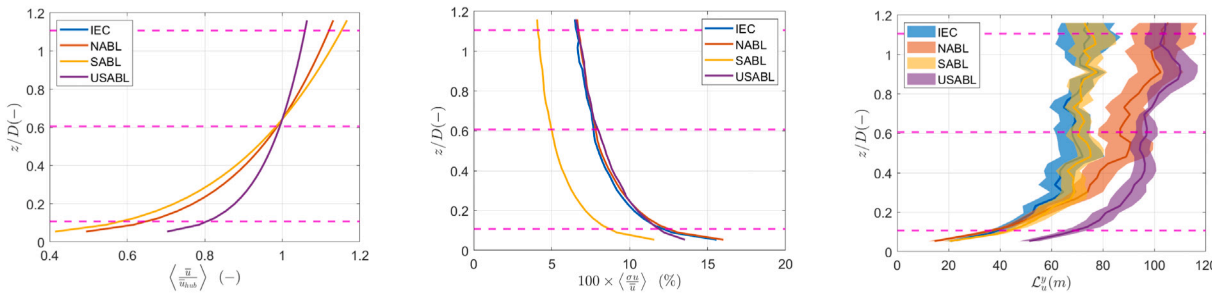

(a) Time-average stream-wise component across non-dimensionalised altitude. The neutral atmosphere and the IEC wind field are overlapping due to the same wind shear.

(b) Standard deviation of stream-wise component across non-dimensionalized altitude.

(c) Span-wise integral length scale of the stream-wise component.

Fig. 2. Synthetic wind field inflow profiles. These are plotted after planar averaging across different cross-stream locations and seed averaging across the six seeds.

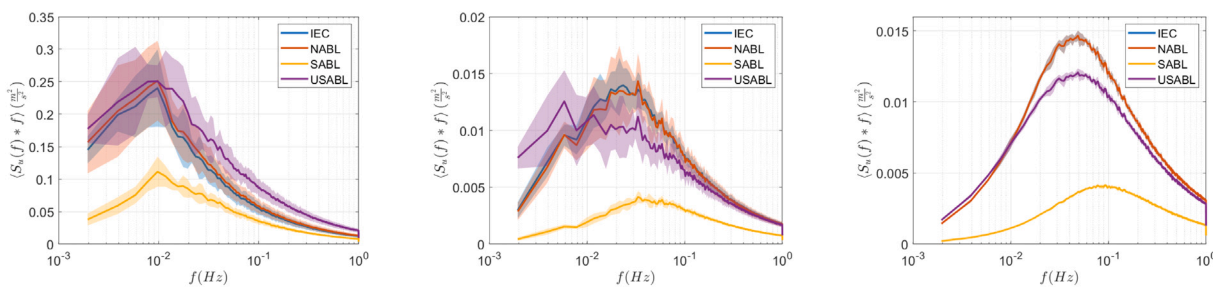

(a) Stream-wise (u) component.

(b) Cross-stream (v) component.

(c) Vertical (w) component.

Fig. 3. Frequency multiplied energy spectrum of velocity components in the synthetic wind field at $z = z_{hub}$, and $U_{hub} = 11.5$ m/s. These are plotted after planar averaging across different cross-stream locations and seed averaging across the six seeds.

are observed among the various atmospheres at different altitudes and separation distances. Once again, the IEC-Kaimal coherence estimate is the lowest. The γ^2_{vv} is generally more important for wake meandering [66–68] than for wind turbine loads. However, the tower top side-side moment or the yaw bearing moment are sensitive to the cross-stream component coherence [60,64].

4. Results and discussions

The aeroelastic simulations using the blade-element momentum theory were conducted on the NREL 5 MW (rated wind speed of 11.4 m/s), and the IEA 22 MW wind turbine (rated wind speed of 11 m/s) in the wind fields generated as per details in Section 3. The open-source software NREL `OpenFAST` [69]—a widely used open-source software developed by the National Renewable Energy Laboratory (NREL)—was used for the aeroelastic simulations. The software has undergone decades of development and rigorous validation by the NREL team and the wider research community (for example, see [70–73]). The results presented in the main study were obtained using the `ElastoDyn` structural module, which does not account for torsional degrees of freedom. While `BeamDyn`—which includes torsional effects—would provide higher-fidelity estimates of absolute load magnitudes (particularly for larger turbines), a comparative study is provided in Appendix A.1. This comparison demonstrates that `ElastoDyn` remains a computationally practical and valid choice for the specific scope and trends investigated here. The NREL `ROSCO` [74] controller with the provided input files was used to regulate the wind turbine control parameters. The aeroelastic simulations were conducted with a time step of 5 ms and ran for 2048 s, with the first 248 s discarded as transient, as detailed earlier. The results of the six seed representatives and the physical understanding of the observed results are detailed in this section. As highlighted earlier, the two chosen wind turbines differ vastly in both their flexibility characteristics and size. Thus, simulations were conducted in both a rigid state (see Appendix A.2) and a flexible state to clearly illustrate the effects.

4.1. Aeroelastic analysis

The wind turbine load channels of interest chosen were the blade-root flapwise bending moment (M_{flap}), tower bottom fore-aft bending moment ($M_{T_{f\text{-}a}}$), and the tower top side-side moment (M_{T_y}).

4.1.1. Instantaneous variation

Firstly, the time-varying signals are shown to illustrate qualitatively the impact of different wind fields. This is shown for one seed of the below-rated operation at $U_{hub} = 6.5$ m/s, as shown in Fig. 6. The first two subfigures present the instantaneous signals of interest for the NREL 5 MW wind turbine and the other two subfigures represent the instantaneous signals of interest for the IEA 22 MW wind turbine. Focussing on Fig. 6(a) and (c), it is evident that M_{flap}(NREL 5 MW), is more noisy than M_{flap}(IEA 22 MW), despite the same sampling rate for the shown signals. This is attributed, first, to the lower rotational speed of the larger wind turbine. This discrepancy also illustrates the effect of rotational sampling on M_{flap}, and the larger turbine acts as a stronger filter for small-scale turbulence. This insight suggests that the largest eddies in the flow are now smaller than the rotor diameter of the larger turbine, and that the larger eddies are sampled slowly, while the largest eddies are larger or comparable to the diameter of the smaller turbine. This effect of rotational sampling is not evident in the $M_{T\text{-}fa}$ shown in Fig. 6(b) and (d). This is because the $M_{T\text{-}fa}$ depends on the global thrust force generated and the dynamic moment generated from the high-energy eddies.

4.1.2. Standard-deviation of loads

Next, the standard deviation of load signals of interest is shown in Fig. 7. The top rows represent the metric of interest for the NREL 5 MW wind turbine, and the bottom rows represent the metric of interest for

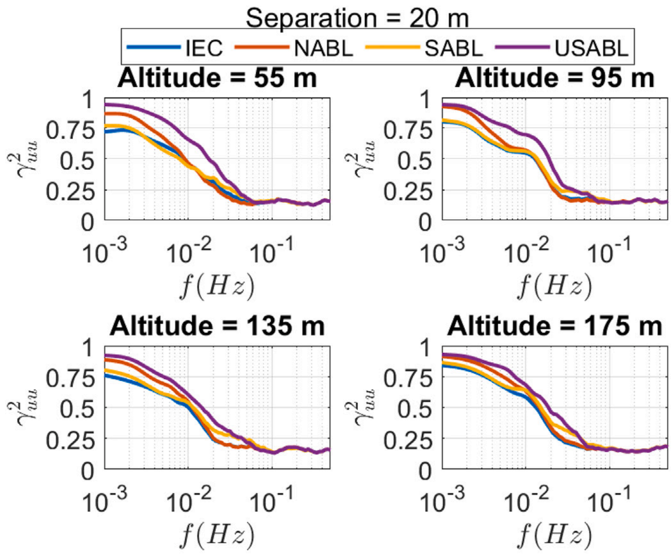

(a) Lateral separation of 20m.

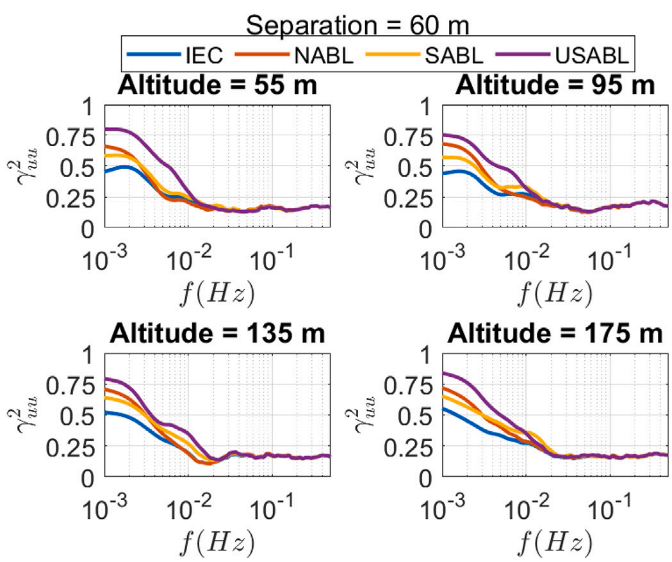

(b) Lateral separation of 60m.

Fig. 4. Magnitude-squared coherence for the stream-wise (u) component at different lateral separations in the synthetic wind field at $z = z_{hub}$ m, and U_{hub} = 11.5 m/s. These are plotted after planar averaging across different cross-stream locations and seed averaging across the six seeds.

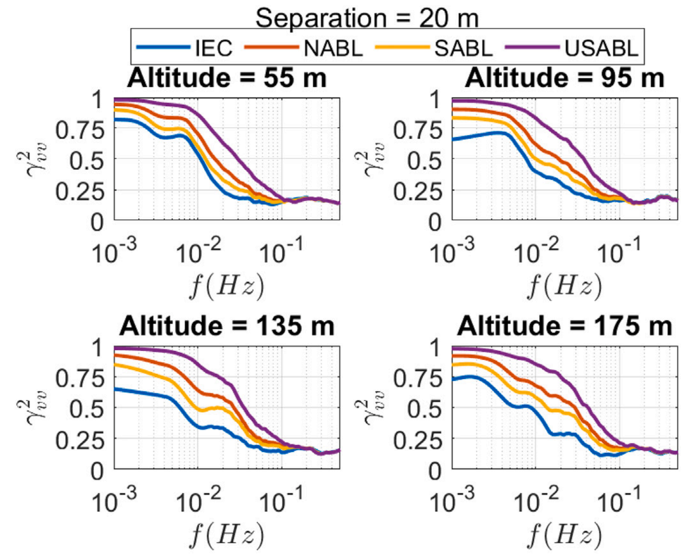

(a) Lateral separation of 20m.

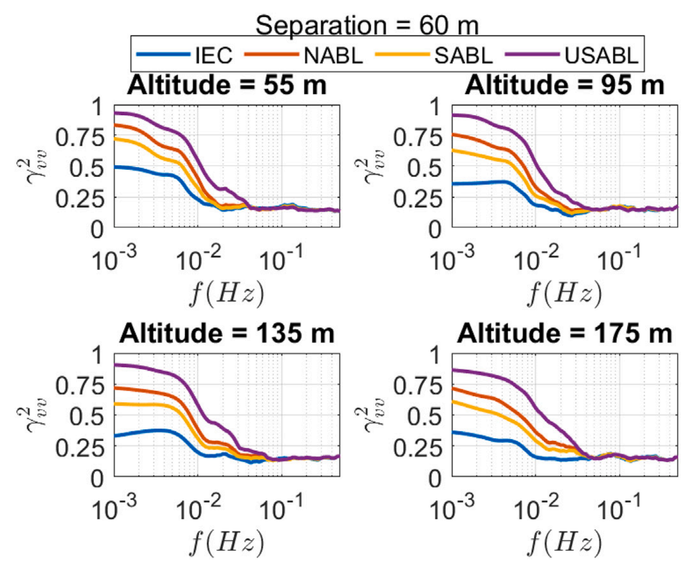

(b) Lateral separation of 60m.

Fig. 5. Magnitude-squared coherence for the cross-stream (v) component at different lateral separations in the synthetic wind field at $z = z_{hub}$ m, and U_{hub} = 11.5 m/s. These are plotted after planar averaging across different cross-stream locations and seed averaging across the six seeds.

the IEA 22 MW wind turbine. Observing Fig. 7(a) and (d), one can note a general trend that the lower wind shear in the USABL leads to a reduced $\sigma_{M_{flap}}$, in comparison to the other wind fields. It is also clear that the impact of this lower wind shear is higher on the larger wind turbine. The relative differences from the IEC wind field are shown in Fig. 8(a), in which up to −35% reduction is seen for the larger wind turbine, while up to −20% for the smaller wind turbine. Between the SABL and IEC wind fields, the expected impact is that higher wind shear leads to greater load deviation, as shown for the large wind turbine. For the smaller turbine, this is not observed, which may be due to the more contrasting effect of high wind shear but lower turbulence. Lastly, between the IEC and the NABL wind field, differences are visible, up to +10%, which implies a higher impact of higher coherence, given that the wind shear, energy spectra, and turbulence are similar in these two wind fields. At this stage, it can be hypothesised that the eddy sizes cause greater non-uniformity for the larger wind turbine, while the smaller turbine experiences more uniform eddies. However, because the synthetic wind field generation uses random phases, it is not entirely accurate to say that the observed differences are due solely to the size or shape of eddies; rather, they are due to a similar phenomenon associated with higher coherence. This can, for instance, be due to the controller dynamics. It can also be stated that the impact of coherence is seen to be overshadowed by the impact of wind shear, since $\sigma_{M_{flap}}(\text{USABL}) << \sigma_{M_{flap}}(\text{NABL})$ while the coherence in the USABL wind fields was higher than in NABL wind fields. The $\sigma_{M_{T\text{-}fa}}$ is shown in Fig. 7(b) and (e) for the 5 MW, and the 22 MW wind turbine, respectively. Generally, the expectation would be that the higher length scales in USABL wind fields lead to higher thrust and thus higher $M_{T\text{-}fa}$. This is evident for both wind turbines. As $M_{T\text{-}fa} \propto T$, the relative differences in thrust (T) are shown as a proxy, in Fig. 8(b). It can be observed that $\sigma_T(\text{USABL}) > \sigma_T(\text{NABL}) > \sigma_T(\text{IEC}) > \sigma_T(\text{SABL})$,

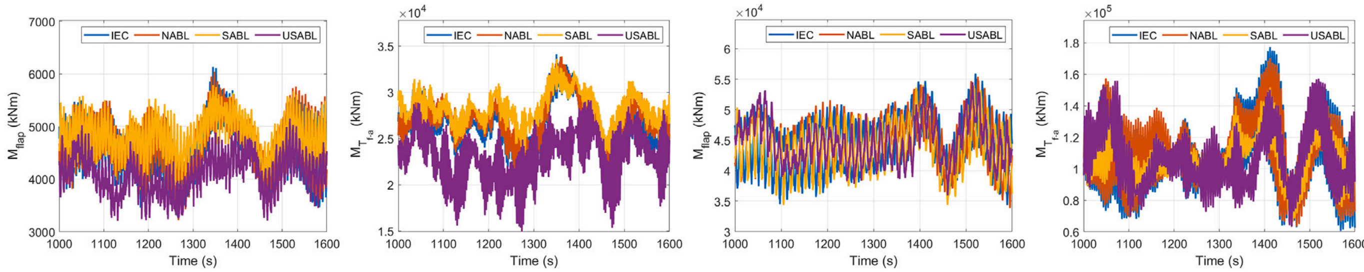

(a) NREL 5 MW :: M_{flap} (b) NREL 5 MW :: $M_{T\text{-}fa}$ (c) IEA 22 MW :: M_{flap} (d) IEA 22 MW :: $M_{T\text{-}fa}$

Fig. 6. Instantaneous global blade and tower loads for the two wind turbines utilised in this study. These are shown for the aeroelastic response in one seed of the synthetic wind field at $U_{hub} = 6.5\,m/s$.

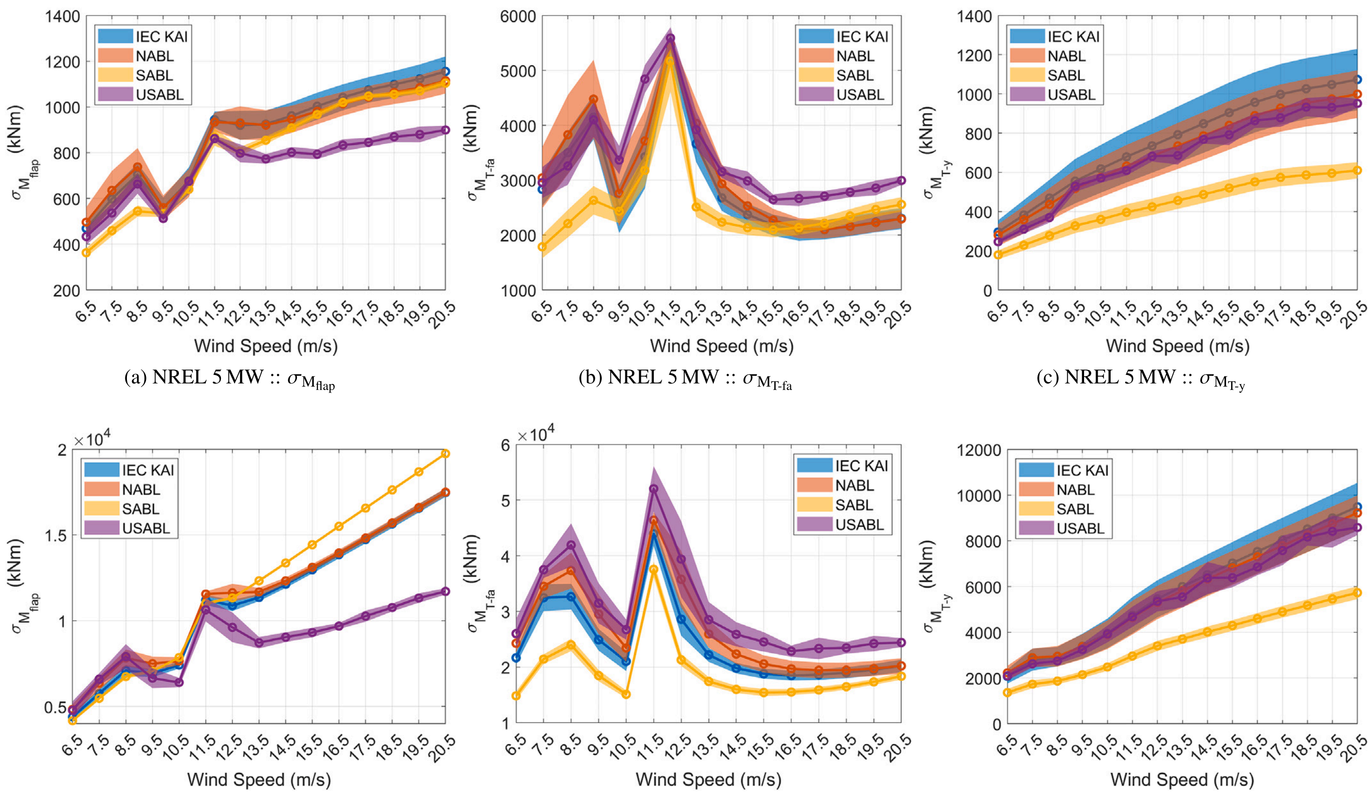

(a) NREL 5 MW :: $\sigma_{M_{flap}}$ (b) NREL 5 MW :: $\sigma_{M_{T\text{-}fa}}$ (c) NREL 5 MW :: $\sigma_{M_{T\text{-}y}}$

(d) IEA 22 MW :: $\sigma_{M_{flap}}$ (e) IEA 22 MW :: $\sigma_{M_{T\text{-}fa}}$ (f) IEA 22 MW :: $\sigma_{M_{T\text{-}y}}$

Fig. 7. Standard deviation of key load signals of the two wind turbines utilised in this study. The top row is for the NREL 5 MW wind turbine and the bottom row is for the IEA 22 MW wind turbine.

and similarly for the $\sigma_{M_{T\text{-}fa}}$. The SABL has the least deviation (−20%) because the turbulence level is half that of the other wind fields, and thus the larger dynamic impact due to coherence is overshadowed. In USABL and NABL, up to +20% difference is observed, and it is more pronounced for the larger wind turbine, despite similar turbulence levels and, in the case of NABL, similar shear, compared to the IEC wind field. This is attributed to the larger length scales and greater coherence. Thus, it should be stressed that despite the same wind shear and turbulence between the IEC and NABL wind field, differences in σ_T of up to +10% are seen for 5 MW wind turbine and +20% for 22 MW wind turbine. This will be further explained by means of wavelet analysis in Section 4.2.

Next, the $\sigma_{M_{T\text{-}y}}$ is shown in Fig. 7(c) and (f), for the 5 MW, and the 22 MW wind turbine, respectively. It can be observed that the most remarkable difference (up to −40%) is for the SABL wind field, in comparison to the other wind fields. This difference is primarily due to lower turbulence levels in the SABL wind field. Although differences in the v-component coherence between the wind fields—and the IEC field, which does not originally define coherence for the v and w components (here the IEC KAI coherence for u component was applied to v component as well)—could in principle introduce deviations, this influence is largely masked by the changes in wind shear. As a result, the effect on the USABL wind fields is negligible.

The differences between the two wind turbines in terms of flexibility and size were noted, which may affect the above-observed relative differences. One more notable difference between the two wind turbine configurations is the geared drivetrain in the NREL 5 MW wind turbine and the direct-drive drivetrain in the IEA 22 MW wind turbine. This distinction could affect the aeroelastic comparison due to variations in structural natural frequency, drivetrain inertia, and mechanical drivetrain stiffness. The first of these is evaluated in the present study through simulations conducted using rigid configurations of both turbines. The

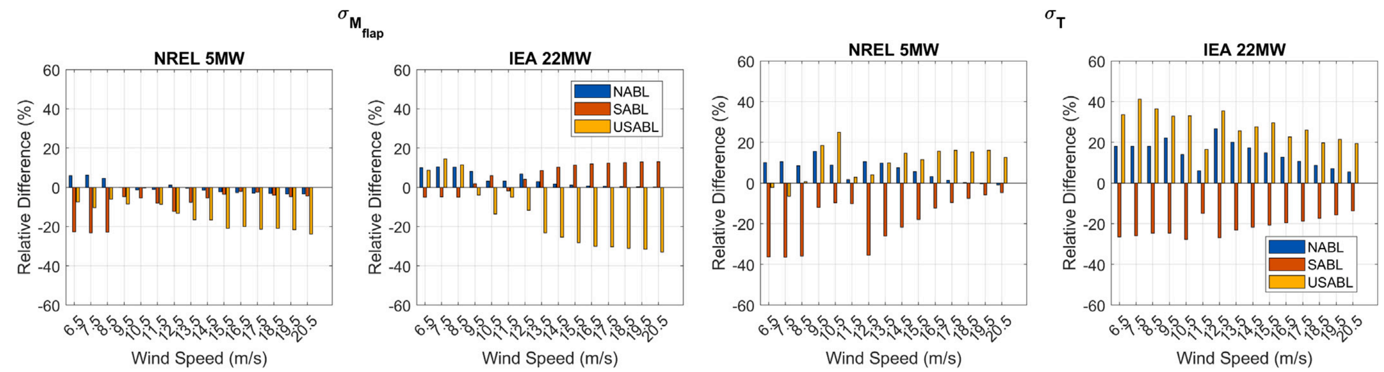

(a) Blade-root flapwise bending moment.

(b) Rotor thrust.

Fig. 8. Relative differences in load standard deviations in different wind fields, in comparison to the IEC Kaimal wind field. The subplots in each sub-figure indicate the relative difference of the load metric for the two, 5 MW and 22 MW wind turbines utilised.

latter two aspects have been previously analysed in [75], where a direct-drive equivalent of the NREL 5 MW turbine was compared with its original geared version in aeroelastic simulations. The results showed differences of $\leq$ 1% in blade and tower fatigue loads, while a more significant difference of $\geq$ 10% was observed only in low-speed shaft fatigue loads for the direct-drive configuration. Since the present study does not consider the low-speed shaft load channel, differences arising from drivetrain topology are not expected to significantly influence the current analysis. Finally, to evaluate the extent to which the observed differences between the two turbines arise from variations in structural flexibility, additional simulations were conducted under a rigid configuration. This is presented in Appendix A.2 where it becomes evident that the effects of flexibility are secondary and the rotor-eddy scale effects are primary, thus strengthening the above-discussed findings.

4.1.3. Damage equivalent loads

Here, the quantifiable insights are provided by assessment of the mean-corrected damage equivalent loads (DELs). The method of [76] was used to calculate the DELs (S_{eq}) using Eq. (20).

$$S_{r,eq} = \left(\frac{\sum_{i=1}^{n} \left(S_{r,i} \frac{S_u - |S_{m,eq}|}{S_u - |S_{m,i}|} \right)^m}{N_{eq}} \right)^{\frac{1}{m}} \tag{20}$$

$S_{r,i}$ is the range (difference between maximum and minimum value) of the ith load cycle, and $S_{m,i}$ is the mean of the ith load cycle. N_{eq} was chosen as 10^7 [42] and $S_{m,eq}$ as 0. Finally, to select S_u, the authors propose evaluating it at different S_{max}/S_u ratios. This is helpful, for instance, because it is difficult to obtain a value of S_u for composite materials. So, the value of S_{max} is used, corresponding to the maximum moment in the respective case, which is different for each wind speed bin. The value of S_{max} which corresponds to the maximum bending moment for the respective wind speed was chosen and $\frac{S_u}{S_{max}} = 0.4$ along with a Wöhler exponent of $m = 10$ for M_{flap} and $m = 4$ for $M_{T_{f\text{-}a}}$ and M_{T_y} [77]. It is worth noting the use of the mean-corrected DEL formulation, unlike other studies that ignore mean loads. The impact of mean-correction is shown to be significant [77].

The absolute DELs for the NREL 5 MW and the IEA 22 MW wind turbine are shown in Fig. 9. It can be seen from Fig. 9(a) and (c), that the $DEL_{M_{flap}}$ is generally lower for the USABL wind field, in comparison to the other wind fields. It is once again noted that this is the case for near-rated to above-rated conditions, and the impact of higher coherence is evident at the below-rated wind speeds. Another observation that can be made is that for the IEA 22 MW wind turbine $DEL_{M_{flap}}(SABL) \approx DEL_{M_{flap}}(NABL)$, instead of it being higher as was found to be the case for $\sigma_{M_{flap}}$. This can be attributed to the mean-load impact on the computed DEL. Between the IEC and the NABL wind field, differences of up to +10% are seen for the NABL wind field, especially at below-rated wind speeds, as shown by the relative differences in Fig. 10(a). This is especially true for the larger IEA 22 MW wind turbine. This will be further analysed by wavelet analysis in Section 4.2.

Next, in regard to the $DEL_{M_{T\text{-}fa}}$ shown in Fig. 9(b) and (d), it can be noted that the trend $DEL_{M_{T\text{-}fa}}(USABL) > DEL_{M_{T\text{-}fa}}(NABL) > DEL_{M_{T\text{-}fa}}(IEC) > DEL_{M_{T\text{-}fa}}(SABL)$. This is linked to the effect of higher length scales for the increased DELs and to the lower turbulence and lower energy content for the reduced DELs in SABL wind fields. The corresponding relative differences are shown for clarity in Fig. 10(b). The trends of $DEL_{M_{T\text{-}y}}$ were similar to $\sigma_{M_{T\text{-}y}}$, and thus, are not shown here for brevity.

4.2. Wavelet analysis

In the preceding section, it was noted that atmospheric stability has a unique impact on wind turbines. It was also found that the impact magnitude is higher for the larger wind turbine. This section explores wavelet analysis of the wind turbine load signal and the hub-height velocity to correlate the two in the frequency-time domain. This unique analysis is hypothesised to reveal the impact of higher coherence in wind fields and provide additional insights in comparison to the typically shown spectral signatures in the frequency space.

4.2.1. Wavelet coherence

Firstly, the wavelet coherence ($R^2_{\mathcal{W}}$) between the $M_{T\text{-}fa}$ and the $U_{rotor,hub}$ is assessed. In the upcoming contours, the first column subfigures show the $R^2_{\mathcal{W}}$ for the NREL 5 MW wind turbine and the second column subfigures show the $R^2_{\mathcal{W}}$ for the IEA 22 MW wind turbine. Here, the first row is for the NABL wind fields, and the second row is for the USABL wind fields, while the SABL and IEC wind field-related results are shown later as quantitative plots. The y-axis indicates the time-period $\tau = 1/f$, with a maximum limit of about 700 s, across different cases. The natural frequency of the first tower fore-aft mode is reported to be 0.32 Hz (viz. $\tau = 3.125$ s) for the NREL 5 MW wind turbine, and 0.16 Hz (viz. $\tau = 6.25$ s) for the IEA 22 MW wind turbine clamped at monopile base. It may also be noted that given the available 1800 s second signal, one would ideally expect a 1/1800 Hz resolution. However, the minimum frequency is determined in practice such that two time standard deviations of the utilised Morlet wavelet span the N-point signal at the coarsest scale.

The results for the same seed in the different cases shown, at a below-rated operation for $U_{\infty,hub} = 6.5$ m/s are presented in Fig. 11. Generally, higher coherence values are observed at longer time periods, while numerous low-time-period areas of high coherence are observed across all

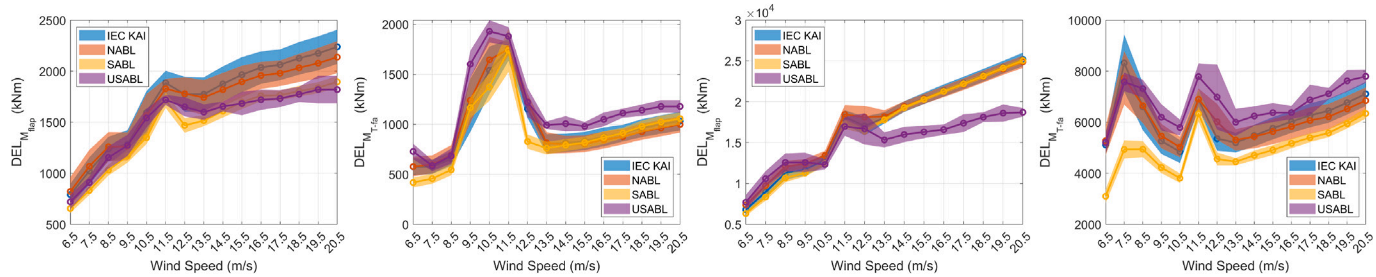

(a) NREL 5MW :: $DEL_{M_{flap}}$ (b) NREL 5MW :: $DEL_{M_{T\text{-}fa}}$ (c) IEA 22MW :: $DEL_{M_{flap}}$ (d) IEA 22MW :: $DEL_{M_{T\text{-}fa}}$

Fig. 9. Damage equivalent loads in the different wind fields and the two wind turbines utilised in this study.

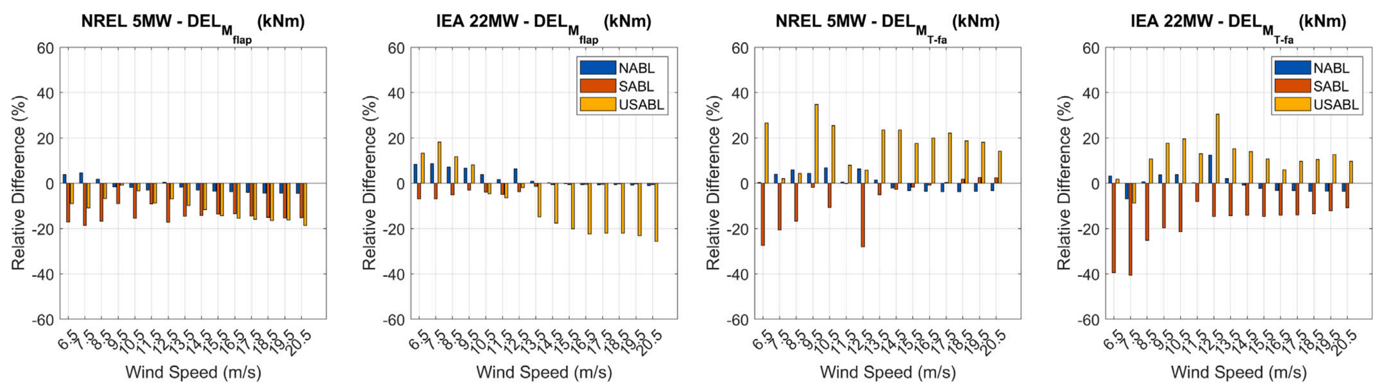

(a) Blade-root flapwise bending moment. (b) Tower base fore-aft bending moment.

Fig. 10. Relative differences in damage equivalent loads in different wind fields, in comparison to the IEC Kaimal wind field. The subplots in each sub-figure indicate the relative difference of the load metric for the two, 5 MW and 22 MW wind turbines utilised.

cases. The latter concerns turbine rotational frequency multiples and, where applicable, natural frequency coupling. However, the former is more important, as these are the highest-energy contributions, leading to a higher aeroelastic impact [28,44].

Focussing on the presented results, row-wise (Fig. 11(a) and (b)), remarkable differences are spotted between the $R^2_{\mathcal{W}}$ in the 5 MW and the 22 MW wind turbine, in the region of large time-scale eddies. For the smaller wind turbine, an almost constant high coherence period is observed over the 1800 s of simulation, whereas for the larger wind turbine this is observed in bursts. Focussing on the presented results, column-wise ((Fig. 11(c) and d)), it can be seen that the higher coherence values in the USABL wind field lead to higher $R^2_{\mathcal{W}}$ in a wider band than in the NABL results. To quantify these values and their variability among seeds, three bands were chosen for statistical analysis as shown in Eq. (21).

$$\begin{aligned} &\text{Band A}: \quad f_{\min} < f_{\text{band}} < 0.01\ \text{Hz} \\ &\text{Band B}: \quad 0.01 < f_{\text{band}} < 0.1\ \text{Hz} \\ &\text{Band C}: \quad 0.1 < f_{\text{band}} < 2\ \text{Hz} \end{aligned} \tag{21}$$

These bands essentially aim to capture the key and unimportant frequencies associated with load response. In [78], a coupling between instantaneous turbine power and the incoming large-scale motion was analysed, and in line with existing literature [79–82], a de-coupling frequency was identified as 1.4 P, where P denotes the turbine rotational frequency. With the ranges mentioned in Section 3, the range for 1.4 P is 0.21 Hz to 0.28 Hz for the NREL 5 MW wind turbine; and 0.07 Hz to 0.17 Hz for the IEA 22 MW wind turbine. Using rounded values of these numbers yields a lower bound of 0.1 Hz for the highest-frequency band, while an upper limit of 2 Hz was selected to approximately align with the 9 P frequency multiple. The lowest frequency band was assigned a lower bound of 0.01 Hz, motivated by indications from [28] that coherent structures in this frequency range contribute significantly to fatigue loads. The band-average and seed-average results are presented in Fig. 12. In Fig. 12, the first column represents the results for the 5 MW wind turbine and the second column represents the results for the 22 MW wind turbine. The lowest subplot in each of these figures shows the $R^2_{\mathcal{W}}$ over Band A, the middle subplot over Band B, and the top subplot over Band C. It becomes clear that the larger structures (lowest freuquency bands) are associated with the highest $R^2_{\mathcal{W}}$, up to 0.9, while the band C has $R^2_{\mathcal{W}}$ up to 0.2, and band B has $R^2_{\mathcal{W}}$ up to 0.5. Focussing on the columns of Fig. 12, it can be noted that the 22 MW wind turbine has the highest coherence in Band A, lower than that of the 5 MW wind turbine. The most prominent $R^2_{\mathcal{W}}$ is for USABL wind fields, while decreasing for different atmospheric stabilities, and the least for the IEC wind fields.

4.2.2. Wavelet cross power

In addition to the $R^2_{\mathcal{W}}$, the cross-wavelet power $|\mathcal{W}^{xy}|$ was evaluated as shown in Fig. 13. The presented result is normalised with the maximum cross-wavelet power in the respective scenario. Once again, it can be noted that the smaller wind turbine experiences a generally longer duration in time of common power between the rotor velocity and the tower fore-aft bending moment than the larger wind turbine. This can be thought of as a quasi-static regime for the smaller wind turbine, such that such high τ regions are not significant to the overall turbine response. On the other hand, the bursts in high common power in the larger wind turbine link these high τ periods to the turbine response time.

4.2.3. Overall remarks

The wavelet analysis revealed the time-frequency correlation between the rotor velocity and the load signal, here, the tower fore-aft bending moment. From the wavelet coherence $R^2_{\mathcal{W}}$, it was seen that the larger 22 MW wind turbine features a different time-frequency signature than the smaller 5 MW wind turbine. The quasi-static regime was

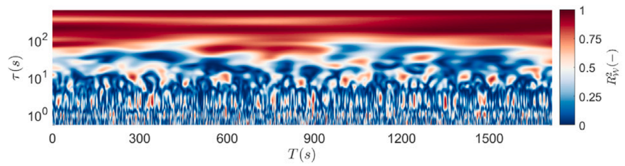
(a) NREL 5MW :: NABL

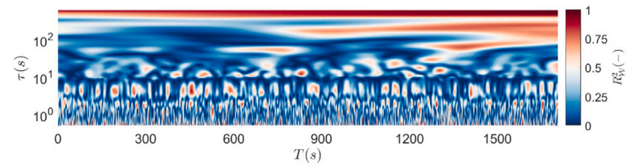
(b) IEA 22MW :: NABL

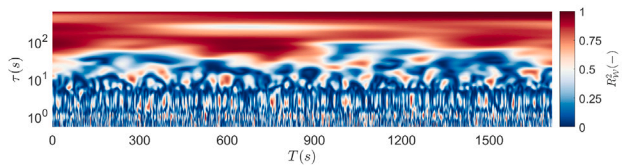
(c) NREL 5MW :: USABL

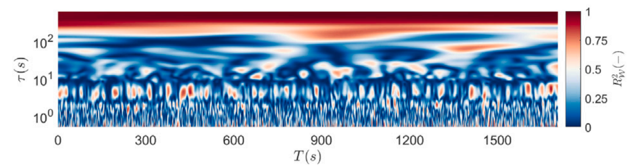
(d) IEA 22MW :: USABL

Fig. 11. Wavelet coherence between wind speed at hub and tower-fore aft bending moment; for one same seed of aeroelastic analysis at below rated operation of $U_{\infty,hub} = 6.5\,m/s$, in different wind fields.

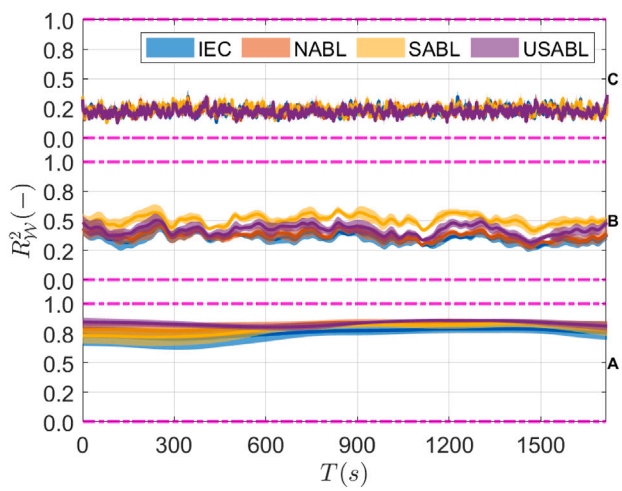

(a) NREL 5 MW

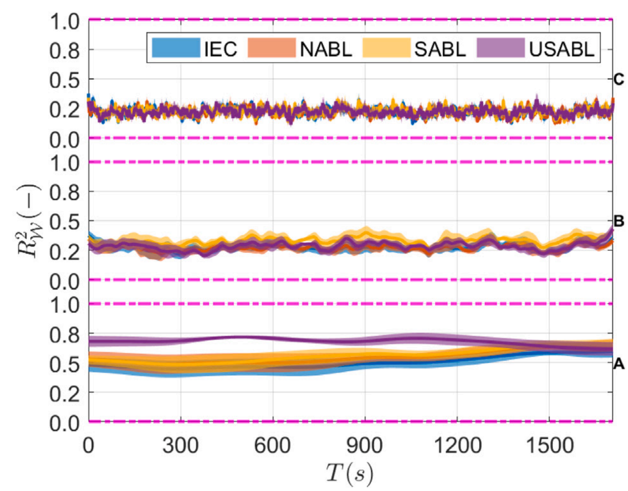

(b) IEA 22 MW

Fig. 12. Band and seed averaged wavelet coherence between wind speed at hub and tower-fore aft bending moment, for aeroelastic analysis at below rated operation of $U_{\infty,hub} = 6.5\,m/s$, in different wind fields. Band A: $f_{min} < f_{band} < 0.01$ Hz, Band B: $0.01 < f_{band} < 0.1$ Hz, Band C: $0.1 < f_{band} < 2$ Hz.

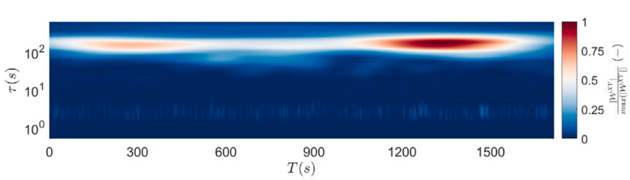
(a) NREL 5 MW :: NABL

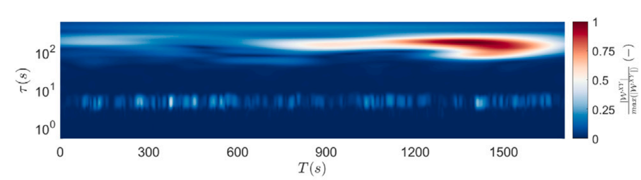
(b) IEA 22 MW :: NABL

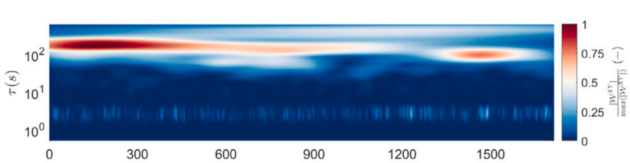
(c) NREL 5 MW :: USABL

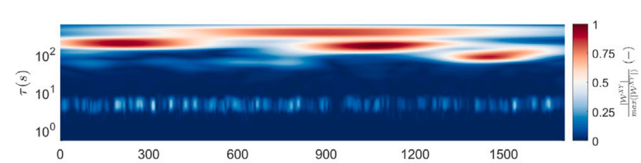
(d) IEA 22 MW :: USABL

Fig. 13. Wavelet cross-power for one same seed of aeroelastic analysis at below rated operation of $U_{\infty,hub} = 6.5\,m/s$, in different wind fields.

found to be wider for the smaller wind turbine and narrower for the larger wind turbine. Large eddies of τ in the order of 10^2 seconds were found to impact the larger wind turbine more than the smaller wind turbine.

It is hypothesised that this observation indicates, among other things, the impact of differences in the inertia of the two turbines and their controller responses. It was noted earlier that the $\Delta(\sigma_T)_{NABL\ vs\ IEC}(22MW) > \Delta(\sigma_T)_{NABL\ vs\ IEC}(5MW)$. Recall also that the differences in IEC and NABL wind field were the coherence formulations and the spectral formulations, specifically because the IEC Kaimal model is different from the original Kaimal model. The latter leads to differences in integral length scales, here, higher integral length scales for the NABL wind field (see Fig. 2(c)). Lastly, given that the $M_{T\text{-fa}}$ is less dependent on wind shear than on turbulence, coherence, and integral length scales [64], it can be said that the $R^2_{\mathcal{W}}(\text{USABL}) > R^2_{\mathcal{W}}(\text{NABL})$ is also due to higher integral length scales and coherence, as inflow turbulence was same for NABL and USABL Fig. 2(b). Finally, one can thus imagine the higher standard deviations in the loads of the larger wind turbine to be linked to the eddy-size hypothesis, namely, that the larger eddies appear more uniform to the smaller wind turbine than to the larger one. Consequently, the differently swept high-energy eddies by the larger rotor lead to more load fluctuations. Both wavelet coherence and wavelet cross-power analysis support this hypothesis. It can be noted that a more robust validation of this hypothesis can be obtained by constructing a frequency map in front of the wind turbine, with coherence assessed using velocity from several points upstream, rather than a single hub-specific velocity. However, it is believed that this analysis would be possible if the eddies are phase-correlated (truly coherent), whereas the spectral synthetic method utilises random phases. The above-discussed analysis was for the case of $U_{\infty,\text{rotor}} = 6.5$ m/s. Similar trends were observed for different wind speeds. Two more representative cases of $U_{\infty,\text{rotor}} = 11.5$ m/s, and of $U_{\infty,\text{rotor}} = 16.5$ m/s, are placed in Appendix B for the interested reader.

5. Conclusions and recommendations

This study focused on addressing the need for better coherence modelling for large offshore wind turbines. More specifically, this study aimed at answering (1) What are the aeroelastic load trends when an empirical stability-dependent coherence model and spectra are employed? (2) How and why does the impact of this model differ between a smaller (5 MW) and a larger (22 MW) wind turbine? One of the primary objectives of this study was to evaluate a tuned coherence model for fast, improved aeroelastic analysis, aiming to achieve computational costs comparable to those of the IEC Kaimal model while enhancing the physical realism of simulated wind fields. This enhanced empirical formulation enables the reproduction of well-known effects of atmospheric stability on wind turbine loads. The novel aspects of this study were discussed as (1) proposing use of measurement-validated coherence model framework suitable for high altitudes upto 287 m and lateral separations upto 241 m for aeroelastic assessment (2) demonstration of scale-dependent aeroelastic response by simulations of a 5 MW and a 22 MW wind turbines (3) use of wavelet analysis for deeper understanding of aeroelastic response.

Synthetic wind fields using spectral approach were generated with a newly proposed stability-dependent coherence model [33] and existing stability-dependent spectral formulations, as well as with the IEC-Kaimal coherence model. The aeroelastic loads using these wind fields were compared by running simulations using NREL `OpenFAST` and NREL `ROSCO` controllers. Two vastly different wind turbines, the NREL 5 MW, and the IEA 22 MW wind turbine were utilised. Aeroelastic simulations were run on six seeds of four types of wind fields: IEC, Neutral (NABL), Stable (SABL), and Unstable (USABL), for 2048 s, allowing for 30 minute analysis timeframe, from $6.5 < U_{\infty,\text{hub}} < 20.5$ m/s in steps of 1 m/s. The damage equivalent loads (DELs), and standard deviation of loads were discussed. The blade-root flapwise bending moment (M_{flap}), tower base fore-aft bending moment ($M_{T\text{-fa}}$), and the tower top side-side moment ($M_{T\text{-ss}}$) were chosen as parameters of interest. Wavelet analysis was employed to physically understand load discrepancies in the time-frequency domain, thereby complementing the typically used Fourier analysis, which focuses solely on the frequency domain.

It was found that the simple coherence and spectral formulations could replicate the well-known effects of atmospheric stability on wind turbine loads. This was in conjunction with the ability of the formulations to yield the physically appropriate integral length scales. It was found that as expected, $\gamma^2(\text{USABL}) > \gamma^2(\text{NABL}) > \gamma^2(\text{SABL}) > \gamma^2(\text{IEC})$, and $\mathcal{L}^u_y(\text{USABL}) > \mathcal{L}^u_y(\text{NABL}) > \mathcal{L}^u_y(\text{IEC}) > \mathcal{L}^u_y(\text{SABL})$. The typically reported $\text{DEL}_{M_{T\text{-fa}}}(\text{USABL}) > \text{DEL}_{M_{T\text{-fa}}}(\text{NABL}) > \text{DEL}_{M_{T\text{-fa}}}(\text{SABL})$ was observed alongside the generally reverse trend or negligible differences for the $\text{DEL}_{M_{\text{flap}}}$. In regard to standard deviations, $\sigma_{M_{\text{flap}}}(\text{SABL}) > \sigma_{M_{\text{flap}}}(\text{NABL}) > \sigma_{M_{\text{flap}}}(\text{IEC}) > \sigma_{M_{\text{flap}}}(\text{USABL}) >$ was clearly evident for the larger 22 MW wind turbine, especially above rated wind speeds, up to +10% in comparison to the IEC wind field, less for the smaller wind turbine. For the thrust, it was found that $\sigma_T(\text{USABL}) > \sigma_T(\text{IEC})$, up to +40% for the larger wind turbine and up to 20 % for the smaller wind turbine. Between NABL and IEC, σ_T was found to be +20% for the large wind turbine and up to +10% for the smaller wind turbine.

Wavelet coherence ($R^2_{\mathcal{W}}$) and cross-wavelet power ($|\mathcal{W}^{xy}|$) were used to link these differences to the intuitive understanding of the effect of larger, high-energy eddies on load fluctuations. From the resulting frequency-time coherence, remarkable differences were observed in the $R^2_{\mathcal{W}}$ between $M_{T\text{-fa}}$ and $U_{\text{rotor,hub}}$, for the smaller and the larger wind turbine. Quasi-static regimes for $\tau = 1/f$ in the order of 10^2 s were seen for the smaller wind turbine as uniform patches of $R^2_{\mathcal{W}}$ throughout the 30 minute simulation. However, for the larger wind turbine, these patches were observed to appear in bursts, which are hypothesised to result from differences in eddy sizes. Efforts were made to isolate the impact of coherence, wind shear, and turbulence on this analysis. Some other reasons for this difference were attributed to differences in inertia between the two wind turbines and to the controller response.

Overall, the relevance of the simple empirical coherence model and existing spectral models was stressed. Future work will consider accessing relevant measurement campaigns to further corroborate the observed differences in loads.

CRediT authorship contribution statement

Nirav Dangi: Writing – original draft, Visualization, Software, Methodology, Investigation, Formal analysis, Data curation, Conceptualization. **Jurij Sodja:** Writing – review & editing, Supervision, Resources, Conceptualization. **Dominic von Terzi:** Writing – review & editing, Supervision, Resources, Conceptualization. **Wei Yu:** Writing – review & editing, Supervision, Resources, Project administration, Funding acquisition, Conceptualization.

Declaration of competing interest

The authors declare that they have no known competing financial interests or personal relationships that could have appeared to influence the work reported in this paper.

Acknowledgements

This research was supported by the Korea Institute of Energy Technology Evaluation and Planning (KETEP) grant, funded by the Korean Government (MOTIE) (20228520020050).

The authors thank the NWO team for the Large Compute Grant [83] (File No. 2025.025) on the Dutch National Supercomputer Snellius. The authors thank SURF (www.surf.nl) for the support in using the Dutch National Supercomputer Snellius.

The authors thank the Delft High Performance Computing Centre [84] for providing access to the computational resources of the DelftBlue supercomputer.

DvT acknowledges support from the MERIDIONAL project, funded by the European Union under the Horizon Europe grant no. 101084216.

Appendix A. Aeroelastic analysis

A.1. Comparison of result trends with higher fidelity structural solver

Throughout the main study, the module `ElastoDyn` of `OpenFAST` was utilised, which neglects the torsional degree of freedom. This choice was expected to only change the absolute values of the load statistics

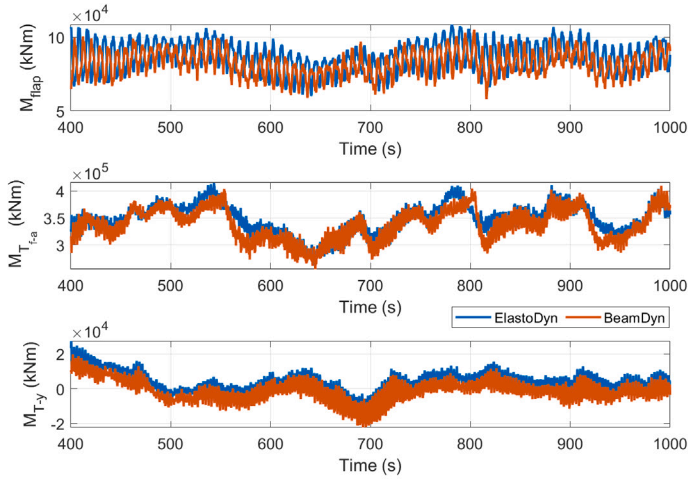

(a) IEC wind field.

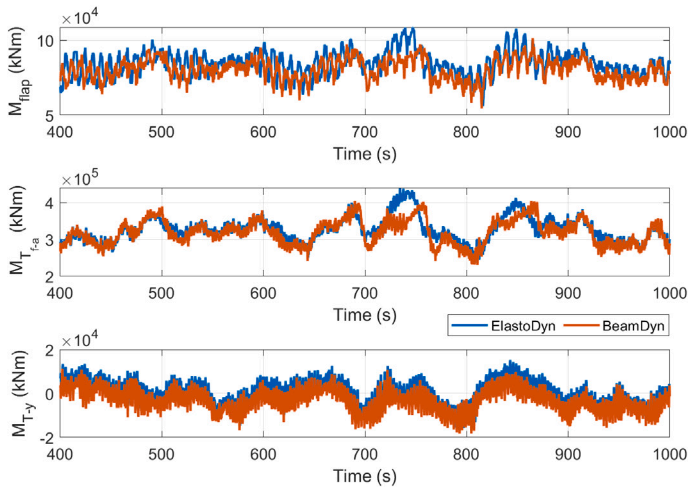

(b) USABL wind field.

Fig. A.14. Instantaneous global blade and tower loads for the IEA 22 MW wind turbine utilised in this study. These are shown for the aeroelastic response in one seed of the synthetic wind field at U_{hub} = 11.5 m/s, in IEC and USABL wind fields. The comparison between the "BeamDyn" module-based result and the "ElastoDyn" module-based result is made.

presented in this study (especially for the IEA 22 MW wind turbine), while the most important trends in relative differences were not expected to change. This expectation is clarified here by comparing the structural results using ElastoDyn and BeamDyn for a subset of the results of the main study. Three key operating regions were chosen ($u_{\infty,hub} \in 6.5, 11.5, 15.5$ m/s), using both ElastoDyn as in the original study, and BeamDyn for the purposes of this sensitivity study. The BeamDyn timestep used for this study was 0.00035 seconds, which is the square root of machine (single) precision and is sufficiently small to avoid convergence issues in BeamDyn. As in the main study, six seeds of wind fields were used to assess aeroelastic response in the IEC, NABL, SABL, and USABL scenarios. Here, a total of $3 \times 6 \times 4 = 72$ BeamDyn simulations were run, for the large IEA 22 MW wind turbine.

First, time-varying signals during a 600 seconds interval are shown in Fig. A.14. The subfigures show the IEC and USABL wind fields for visualisation purposes at the rated operating condition. The results are plotted for the three load channels of interest, as in the main study:

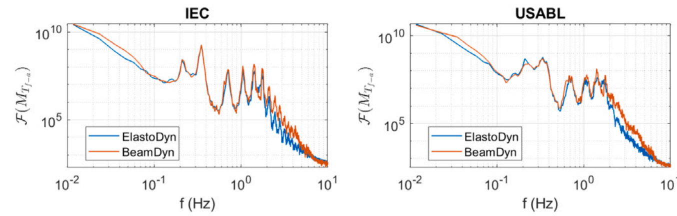

(a) Tower fore-aft bending moment.

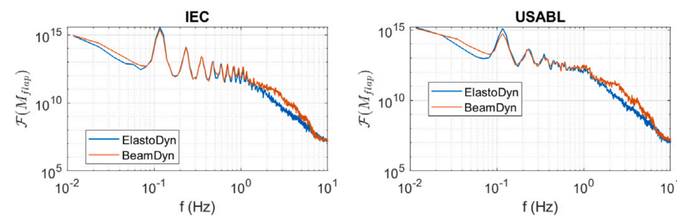

(b) Blade root flapwise bending moment.

Fig. A.15. Energy spectrum of the tower fore-aft bending moment and blade root flapwise bending moment for the IEA 22 MW wind turbine utilised in this study. These are shown for the aeroelastic response in one seed of the synthetic wind field at U_{hub} = 11.5 m/s, in IEC and USABL wind fields. The comparison between the "BeamDyn" module-based result and the "ElastoDyn" module-based result is made.

$M_{T_{f-a}}$, M_{flap}, M_{T-y} (tower fore-aft bending moment, blade root flapwise bending moment, and tower top side-side moment), in the different subplots of each subfigure. From these instantaneous visualisations, it is evident that the load ranges and qualitative frequency content are similar across the two structural solvers.

This aspect was further analysed by Fourier transform ($\mathcal{F}$) of the load channels, of which, the results for $\mathcal{F}(M_{T_{f-a}})$ and $\mathcal{F}(M_{flap})$ are presented in each subfigure of Fig. A.15. The subplots are for the IEC and USABL wind fields. These visualisations confirm that the major low-frequency content and rotational frequency peaks of the load channels are captured similarly in both structural solvers. The only remarkable difference is spotted for the high-frequency (here, $\geq$ 1 Hz) part of the spectrum, which is not a dominant contributor to (fatigue) loads.

Lastly, the most important metric for this study was the relative difference in load standard deviation with respect to the IEC Kaimal model-based wind field. This metric is plotted in Fig. A.16, in same fashion as the main study. For visualisation purposes, the $\sigma_{M_{flap}}$ and $\sigma_{M_{T_{f-a}}}$ are plotted as bars with seed-averaged relative differences from the IEC Kaimal model-based wind field, using both ElastoDyn (darker shade bars) and BeamDyn (lighter dotted shade bars). The data indicate that the choice of structural solver does not significantly alter the relative difference trends, especially when looking at the trends from the benchmark wind field.

A.2. Assessing effects of differences in flexibility

The relative differences in the standard deviation of loads, in comparison to the IEC wind field, were shown in Fig. 8. These results were for the flexible wind turbine. The greater impact on the larger wind turbine was evident; thus, one may question whether this is due to the different flexibility characteristics of the larger 22 MW wind turbine compared to the smaller 5 MW wind turbine. To illustrate that the effects of flexibility are secondary and those of coherence and integral length scales are primary, aeroelastic simulations were also conducted for a rigid configuration of the wind turbines. The resulting differences in loads, in comparison to the IEC wind field, are shown in Fig. A.17.

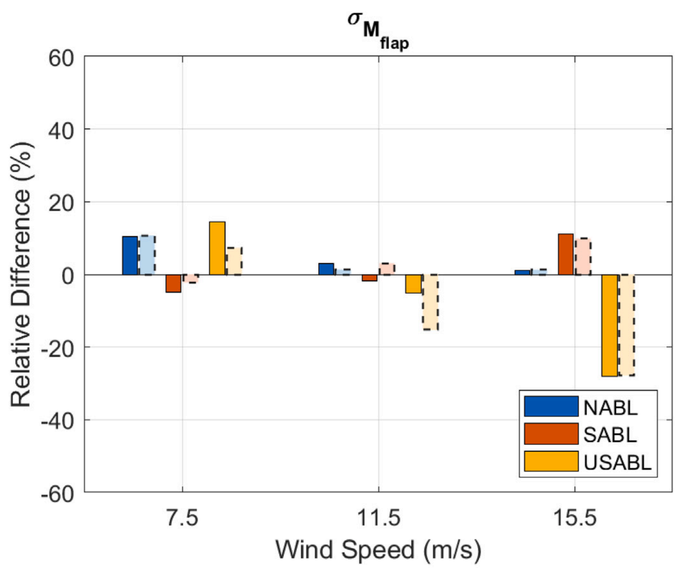

(a) Blade-root flapwise bending moment.

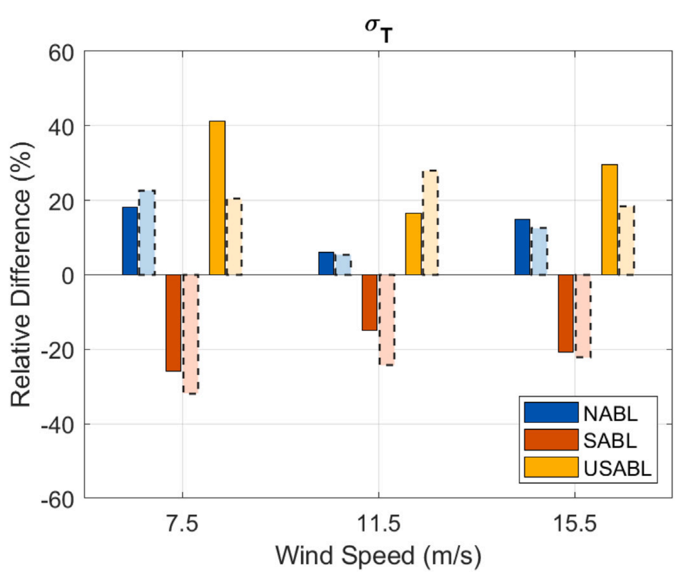

(b) Rotor thrust.

Fig. A.16. Relative differences in load standard deviations in different wind fields, in comparison to the IEC Kaimal wind field. The relative differences of the load metric for the 22 MW wind turbine are shown. The lighter dotted shade bar represents the "`BeamDyn`" module-based result, while the darker shade bars represent the "`ElastoDyn`" module-based result.

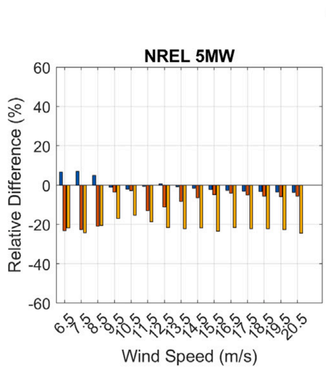

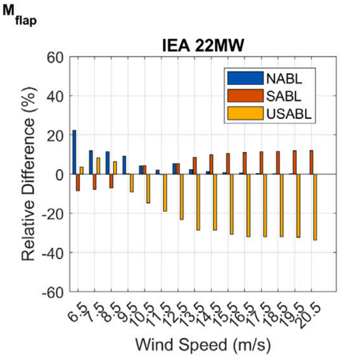

(a) Blade-root flapwise bending moment.

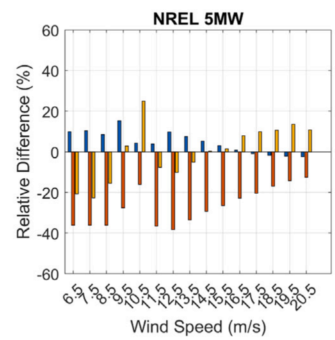

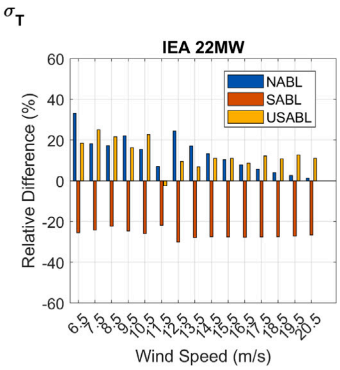

(b) Rotor thrust.

Fig. A.17. Relative differences in load standard deviations in different wind fields, in comparison to the IEC Kaimal wind field. The subplots in each sub-figure indicate the relative difference of the load metric for the two, *RIGID* 5 MW and 22 MW wind turbines utilised.

Appendix B. Wavelet analysis

The wavelet analysis was presented in Section 4.2 for the below-rated operation at $U_{\infty,hub}$ = 6.5 m/s. In this section, similar result visualizations are placed for two more wind speed regimes, $U_{\infty,hub}$ = 11.5 m/s in Fig. B.18 to Fig. B.20, and $U_{\infty,hub}$ = 16.5 m/s, in Fig. B.21 to Fig. B.23.

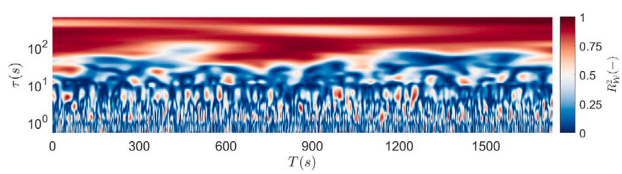

(a) NREL 5MW :: NABL

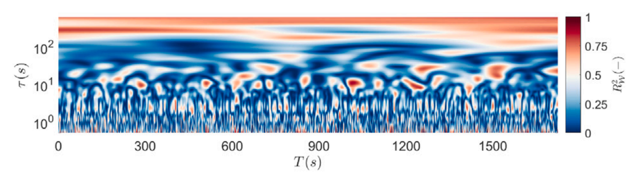

(b) IEA 22MW :: NABL

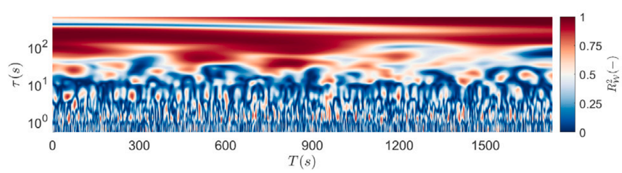

(c) NREL 5MW :: USABL

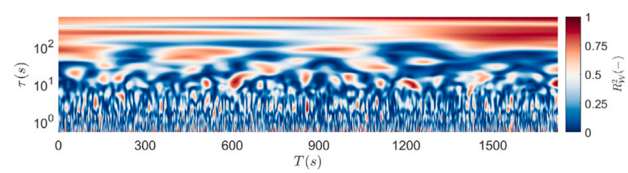

(d) IEA 22MW :: USABL

Fig. B.18. Wavelet coherence between wind speed at hub and tower-fore aft bending moment; for one same seed of aeroelastic analysis at below rated operation of $U_{\infty,hub}$ = 11.5 m/s, in different wind fields.

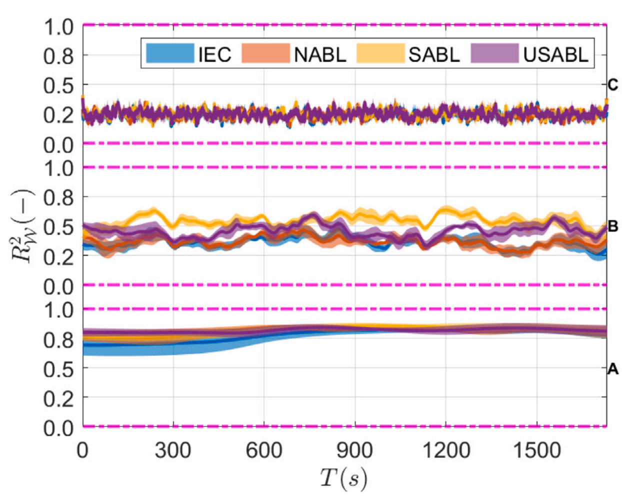

(a) NREL 5 MW

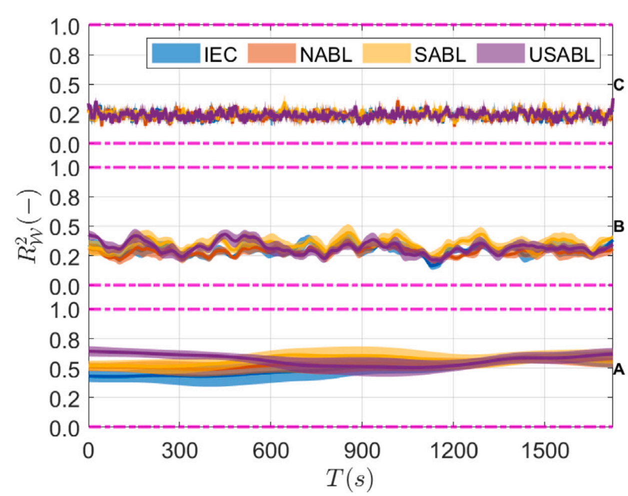

(b) IEA 22 MW

Fig. B.19. Band and seed averaged wavelet coherence between wind speed at hub and tower-fore aft bending moment, for aeroelastic analysis at below rated operation of $U_{\infty,hub}$ = 11.5 m/s, in different wind fields. Band A: $f_{min} < f_{band} < 0.01$ Hz, Band B: $0.01 < f_{band} < 0.1$ Hz, Band C: $0.1 < f_{band} < 2$ Hz.

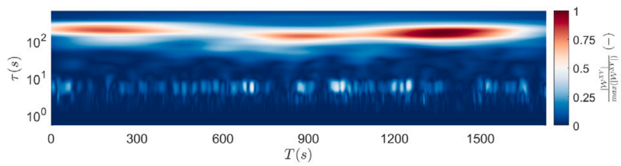

(a) NREL 5 MW :: NABL

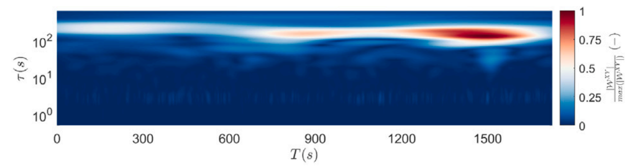

(b) IEA 22 MW :: NABL

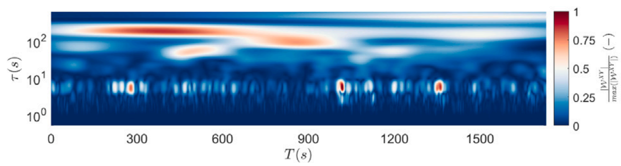

(c) NREL 5 MW :: USABL

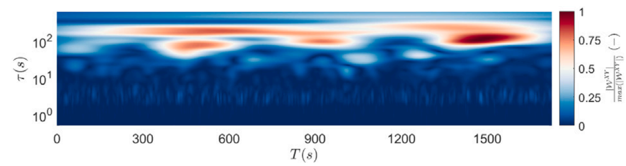

(d) IEA 22 MW :: USABL

Fig. B.20. Wavelet cross-power for one same seed of aeroelastic analysis at below rated operation of $U_{\infty,hub} = 11.5$ m/s, in different wind fields.

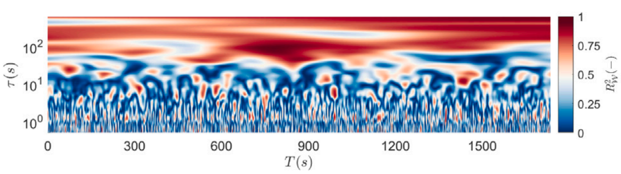

(a) NREL 5MW :: NABL

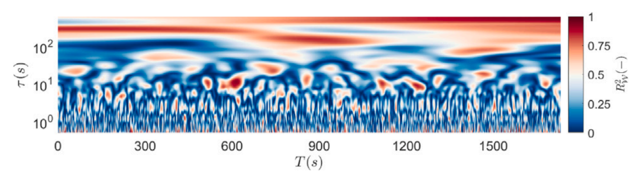

(b) IEA 22MW :: NABL

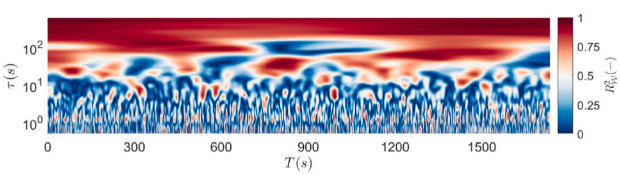

(c) NREL 5MW :: USABL

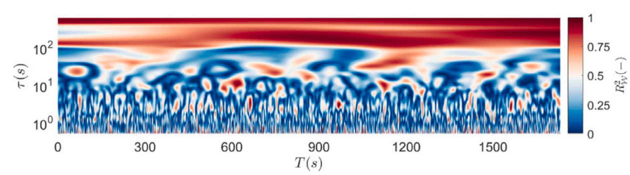

(d) IEA 22MW :: USABL

Fig. B.21. Wavelet coherence between wind speed at hub and tower-fore aft bending moment; for one same seed of aeroelastic analysis at below rated operation of $U_{\infty,hub} = 16.5$ m/s, in different wind fields.

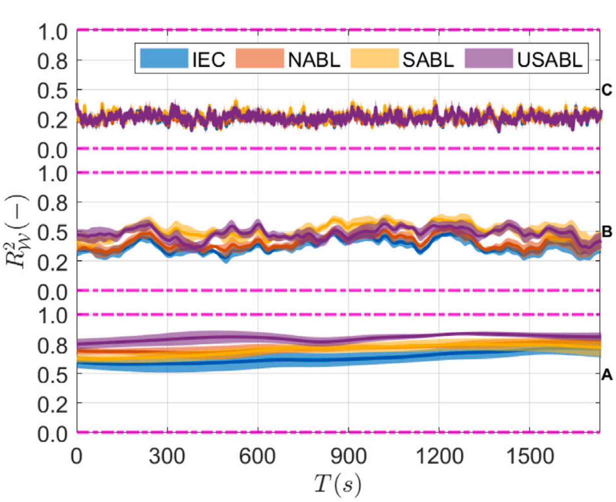

(a) NREL 5 MW

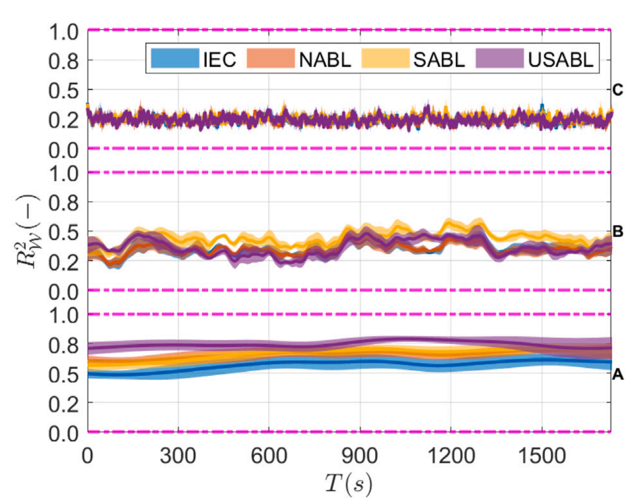

(b) IEA 22 MW

Fig. B.22. Band and seed averaged wavelet coherence between wind speed at hub and tower-fore aft bending moment, for aeroelastic analysis at below rated operation of $U_{\infty,hub} = 16.5$ m/s, in different wind fields. Band A: $f_{min} < f_{band} < 0.01$ Hz, Band B: $0.01 < f_{band} < 0.1$ Hz, Band C: $0.1 < f_{band} < 2$ Hz.

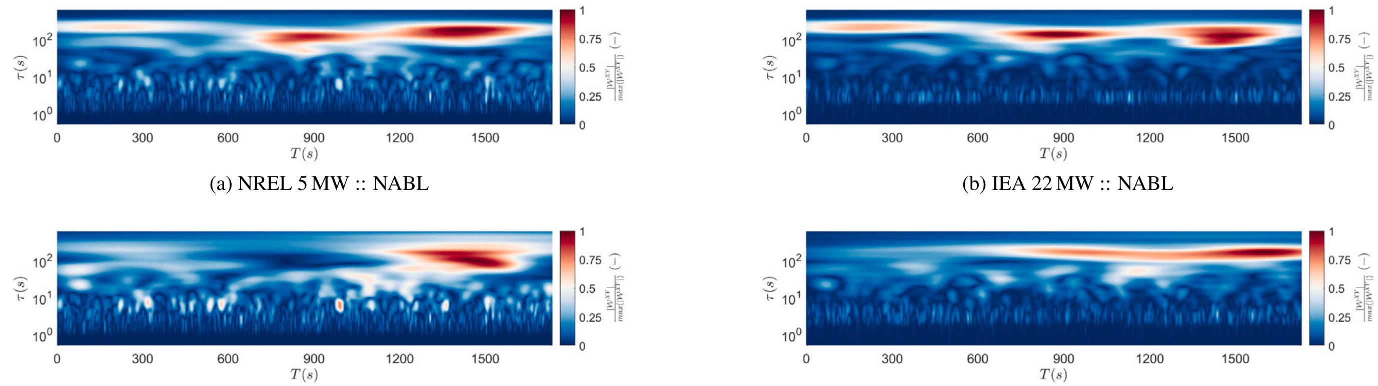

(a) NREL 5 MW :: NABL

(b) IEA 22 MW :: NABL

(c) NREL 5 MW :: USABL

(d) IEA 22 MW :: USABL

Fig. B.23. Wavelet cross-power for one same seed of aeroelastic analysis at below rated operation of $U_{\infty,hub}$ = 16.5 m/s, in different wind fields.

Data availability

Data will be made available on request.

References

[1] Jung C, Schindler D. The properties of the global offshore wind turbine Fleet. Renew Sustain Energy Rev Oct 2023;186:113667. 1364-0321. https://doi.org/10.1016/J.RSER.2023.113667
[2] Jung C, Sander L, Schindler D. Future global offshore wind energy under climate change and advanced wind turbine technology. Energy Convers Manag Dec 2024;321:119075. 0196-8904. https://doi.org/10.1016/J.ENCONMAN.2024.119075
[3] Europe W, Costanzo G, Brindley G, Tardieu P. Wind energy in Europe: 2024 statistics and the outlook for 2025-2030. Tech. rep Brussels: Wind Europe; 2024. https://windeurope.org/data/products/wind-energy-in-europe-2024-statistics-and-the-outlook-for-2025-2030/.
[4] International Electrotechnical Commission (IEC). IEC 61400-1:2019; 2019. https://webstore.iec.ch/publication/26423.
[5] International Electrotechnical Commission (IEC). IEC 61400-3-1:2019 – IEC webstore; 2019. https://webstore.iec.ch/publication/29360.
[6] International Electrotechnical Commission (IEC). IEC 61400-13 – IEC webstore; 2015. https://webstore.iec.ch/en/publication/23971.
[7] Mann J. The spatial structure of neutral atmospheric surface-layer turbulence. J Fluid Mech 1994;273:141–68. 0022-1120. https://orbit.dtu.dk/en/publications/the-spatial-structure-of-neutral-atmospheric-surface-layer-turbul.
[8] Mann J. Wind field simulation. Probabilistic Eng Mech Oct 1998;13(4):269–82. 0266-8920. https://doi.org/10.1016/S0266-8920(97)00036-2
[9] Kaimal JC, Wyngaard JC, Izumi Y, Coté OR. Spectral characteristics of surface-layer turbulence. Q J R Meteorol Soc Jul 1972;98(417):563–89. 1477-870X. https://doi.org/10.1002/QJ.49709841707
[10] Robert Thresher WEH, Smith CE, Jafarey N, Lin SR. Modeling the response of wind turbines to atmospheric turbulence; Aug, 1981. https://doi.org/10.2172/6811573
[11] Davenport AG. The application of statistical concepts to the wind loading of structures. Proceedings of the Institution of Civil Engineers 1961;19(4):449–72. https://doi.org/10.1680/iicep.1961.11304
[12] Cheynet E, Jakobsen JB, Reuder J. Velocity spectra and coherence estimates in the marine atmospheric boundary layer. Bound-Layer Meteorol Dec 2018;169(3):429–60. 15731472. https://doi.org/10.1007/S10546-018-0382-2/TABLES/3. https://link.springer.com/article/10.1007/s10546-018-0382-2.
[13] Barthelmie RJ. The effects of atmospheric stability on coastal wind climates. Meteorol Appl 1999;6(1):39–47. https://doi.org/10.1017/S1350482799000961. https://rmets.onlinelibrary.wiley.com/doi/abs/10.1017/S1350482799000961.
[14] Sathe A, Gryning S-E, a AP. Comparison of the atmospheric stability and wind profiles at two wind farm sites over a long marine fetch in the North sea. Wind Energy 2011;14(6):767–80. https://doi.org/10.1002/we.456
[15] Monin AS, Obukhov AM. Basic laws of turbulent mixing in the surface layer of the atmosphere. Geophys. Inst. Acad. Sci. USSR 1954;24(151):163–87. https://gibbs.science/efd/handouts/monin_obukhov_1954.pdf.
[16] Obukhov AM. Turbulentnost' v temperaturnoj – neodnorodnoj atmosfere (turbulence in an atmosphere with a non-uniform temperature). Trudy Inst. Theor. Geofiz AN SSSR1 1946;95–115.
[17] Obukhov AM. Turbulence in an atmosphere with a non-uniform temperature. Bound-Layer Meteorol Mar 1971;2(1):7–29. 00068314. https://doi.org/10.1007/BF00718085/METRICS. https://link.springer.com/article/10.1007/BF00718085.
[18] Bernhardt K-H. Zur interpretation der monin-obuchovschen länge. Meteorol Z Nov 1995;4(2):81–2. https://doi.org/10.1127/metz/4/1992/81
[19] Foken T. 50 years of the monin-obukhov similarity theory. Bound-Layer Meteorol Jun 2006;119(3):431–47. 00068314. https://doi.org/10.1007/S10546-006-9048-6/METRICS. https://link.springer.com/article/10.1007/s10546-006-9048-6.
[20] Stull R. Practical meteorology: an algebra-based survey of atmospheric science; 2017. https://www.eoas.ubc.ca/books/Practical_Meteorology/.
[21] Højstrup J. Velocity spectra in the unstable planetary boundary Layer. English. Journal of Atmospheric Sciences 1982;39(10):2239–48.
[22] Olesen HR, Larsen SE, Højstrup J. Modelling velocity spectra in the lower part of the planetary boundary layer. Bound-Layer Meteorol 1984;29(3):285–312. 15731472. https://doi.org/10.1007/BF00119794/METRICS. https://link.springer.com/article/10.1007/BF00119794.
[23] Sathe A, Bierbooms W. Influence of different wind profiles due to varying atmospheric stability on the fatigue life of wind turbines. J Phys Conf Ser 2007;75(1):012056. 1742-6596. https://doi.org/10.1088/1742-6596/75/1/012056
[24] Sathe A, Mann J, Barlas TK, Bierbooms WAAM, Van Bussel GJW. Atmospheric stability and its influence on wind turbine loads. In: TORQUE: the science of making torque from wind. APA; 2012.
[25] Doubrawa P, Matthew J, Marte Godvik C, Sirnivas S. Load response of a floating wind turbine to turbulent atmospheric flow. Appl Energy May 2019;242:1588–99. 0306-2619. https://doi.org/10.1016/J.APENERGY.2019.01.165
[26] Putri RM, Cheynet E, Obhrai C, Jakobsen JB. Turbulence in a coastal environment: the case of vindeby. Wind Energy Sci Aug 2022;7(4):1693–710. 23667451. https://doi.org/10.5194/WES-7-1693-2022
[27] Putri RM, Obhrai C. Wind-induced response of an offshore wind turbine under non-neutral conditions: a comparison with hywind Scotland. J Phys Conf Ser Nov 2022;2362(1):012031. 1742-6596. https://doi.org/10.1088/1742-6596/2362/1/012031. https://iopscience.iop.org/article/10.1088/1742-6596/2362/1/012031%20https://iopscience.iop.org/article/10.1088/1742-6596/2362/1/012031/meta.
[28] Dangi N, Sodja J, Ferreira CS O, Wei Y. The effect of turbulent coherent structures in atmospheric flow on wind turbine loads. Renew Energy 2025;241:122248. 0960-1481. https://doi.org/10.1016/j.renene.2024.122248. https://www.sciencedirect.com/science/article/pii/S0960148124023164.
[29] Guo F, a AP, Gao Z. Effects of turbulence inhomogeneity and atmosphere stability on the aeroelastic response of the IEA 22 MW wind turbine. Renew Energy Jan 2026;256:124384. 0960-1481. https://doi.org/10.1016/J.RENENE.2025.124384
[30] Guo F, Gao Z. Load and response analysis of the IEA 22 MW monopile wind turbine considering marine atmospheric turbulence characteristics. J Ocean Eng Sci Apr 2026;11(2):667–80. 2468-0133. https://doi.org/10.1016/J.JOES.2026.01.002
[31] Syed AH, Mann J. A model for low-frequency, anisotropic wind fluctuations and coherences in the marine atmosphere. Boundary-Layer Meteorology 2024 Jan 2024;190(1):1. 1573-1472. https://doi.org/10.1007/S10546-023-00850-W. https://link.springer.com/article/10.1007/s10546-023-00850-w.
[32] Patel A, Mann J, Sjöholm M, Zinck K, Raj K. Comparison of measured and simulated fatigue loads on a multi-megawatt wind turbine. Wind Energy Sci Apr 2026;11(4):1147–62. 2366-7443. https://doi.org/10.5194/WES-11-1147-2026. https://wes.copernicus.org/articles/11/1147/2026/.
[33] Dangi NS, Sodja J, von Terzi D, Wei Y. Atmospheric turbulence modelling for very large wind turbines. AIAA SCITECH 2026 Forum Jan 2026. https://doi.org/10.2514/6.2026-0860
[34] Patel A, Mann J, Sjöholm M, Thorsen GR, Simon E, Syed AH, Hung L-Y, Gottschall J. Trans experiment post-processed data. DTU data repository Feb 2025. https://doi.org/10.11583/DTU.28390181.v1. https://data.dtu.dk/articles/dataset/Trans_experiment_post-processed_data/28390181.
[35] Patel A, Mann J, Sjöholm M, Thorsen GR, Syed AH, Simon EI, Hung LY, Gottschall J. LiDAR observations of turbulence for tall offshore wind turbines. J Fluid Mech Jan 2026;1028:A9. 0022-1120. https://doi.org/10.1017/JFM.2025.11103. https://www.cambridge.org/core/journals/journal-of-fluid-mechanics/article/lidar-observations-of-turbulence-for-tall-offshore-wind-turbines/597DD064C35574F684DE5F5EF4C5A3E8.
[36] Jonkman J, Butterfield S, Musial W, Scott G. Definition of a 5-MW reference wind turbine for offshore system development; 2009. http://www.osti.gov/bridge.
[37] Zahle F, Barlas T, Lønbæk K, Bortolotti P, Zalkind D, Wang L, Labuschagne C, Sethuraman L, Barter G. Definition of the IEA wind 22-megawatt offshore reference

wind turbine; 2024). https://doi.org/10.11581/DTU.00000317. https://backend.orbit.dtu.dk/ws/files/357327260/iea-22-280-rwt-report.pdf.

[38] Xiaohua W. Inflow turbulence generation methods. Annu Rev Fluid Mech 2017. https://doi.org/10.1146/annurev-fluid-010816-060322. https://cfd.spbstu.ru/agarbaruk/doc/2017_Wu_Inflow%20Turbulence%20Generation%20Methods.pdf.

[39] Benoit ' Commandant. Note sur une méthode de résolution des équations normales provenant de l'application de la MéThode des moindres carrés a un système d'équations linéaires en nombre inférieur a celui des Inconnues. -Application de la méthode a la résolution d'un système defini d'éQuations LinéAires (procédé du commandant cholesky). Bulletin Géodésique Apr 1924;2(1):67–77. 00074632. https://doi.org/10.1007/BF03031308/METRICS. https://link.springer.com/article/10.1007/BF03031308.

[40] Jonkman BJ. TurbSim user's guide. National renewable energy laboratory (NREL). Tech. rep. Oct 2014. www.nrel.gov/publications.

[41] Businger JA, Wyngaard JC, Izumi Y, Bradley EF. Flux-profile relationships in the atmospheric surface layer. Journal of Atmospheric Sciences 1971;28(2):181–9.

[42] Holtslag MC, Bierbooms WAAM, Van Bussel GJW. Estimating atmospheric stability from observations and correcting wind shear models accordingly. J Phys Conf Ser Dec 2014;555(1):012052. 1742-6596. https://doi.org/10.1088/1742-6596/555/1/012052

[43] Kristensen L, Jensen NO. Lateral coherence in isotropic turbulence and in the natural wind. Bound-Layer Meteorol 1979;17(3):353–73. 15731472. https://doi.org/10.1007/BF00117924/METRICS. https://link.springer.com/article/10.1007/BF00117924.

[44] Nybø A, Nielsen FG, Godvik M. Quasi-static response of a bottom-fixed wind turbine subject to various incident wind fields. Wind Energy Dec 2021;24(12):1482–500. 1099-1824. https://doi.org/10.1002/WE.2642. https://onlinelibrary.wiley.com/doi/full/10.1002/we.2642.

[45] Welch PD. The use of fast Fourier transform for the estimation of power spectra: a method based on time averaging over short, modified periodograms. IEEE Trans Audio Electroacoust 1967;15(2):70–3. 00189278. https://doi.org/10.1109/TAU.1967.1161901

[46] Saranyasoontorn K, Manuel L, Veers PS. A comparison of standard coherence models for inflow turbulence with estimates from field measurements. J Sol Energy Eng Nov 2004;126(4):1069–82. 0199-6231. https://doi.org/10.1115/1.1797978

[47] Panofsky HA, Dutton JA. Atmospheric turbulence: models and methods for engineering applications. New York: Wiley; 1984. p. 219.

[48] Torrence C, Compo GP. A practical guide to wavelet analysis. Bull Am Meteorol Soc 1998;79(1):61–78.

[49] Grinsted A, Moore JC, Jevrejeva S. Application of the cross wavelet transform and wavelet coherence to geophysical time series. Nonlinear Process Geophys 2004;11(5/6):561–6. https://doi.org/10.5194/npg-11-561-2004. https://npg.copernicus.org/articles/11/561/2004/.

[50] Crowley PM. A guide to wavelets for economists. J Econ Surv 2007;21(2):207–67. https://doi.org/10.1111/j.1467-6419.2006.00502.x

[51] Aguiar-Conraria L, Martins MMF, Soares MJ. The yield curve and the macro-economy across time and frequencies. J Econ Dyn Control 2012;36(12):1950–70. 0165-1889. https://doi.org/10.1016/j.jedc.2012.05.008. https://www.sciencedirect.com/science/article/pii/S016518891200125X.

[52] Foufoula-Georgiou E, Kumar P. Wavelet analysis in geophysics: an introduction. In: Foufoula-Georgiou E, Kumar P, editors. Wavelets in geophysics, vol. 4. Wavelet Analysis and Its Applications. Academic Press; 1994. p. 1–43. https://doi.org/10.1016/B978-0-08-052087-2.50007-4, https://www.sciencedirect.com/science/article/pii/B9780080520872500074.

[53] Gurley K, Kareem A. Applications of wavelet transforms in earthquake, wind and ocean engineering. Eng Struct 1999;21:149–67. https://api.semanticscholar.org/CorpusID:18512036.

[54] Kelley ND, Jonkman BJ, Scott GN, Bialasiewicz JT, Redmond LS. Impact of coherent turbulence on wind turbine aeroelastic response and its simulation: Preprint. English. In: United States; 2005. https://www.osti.gov/biblio/15020042%20https://www.osti.gov/servlets/purl/15020042.

[55] Holtslag MC, Bierbooms WAAM, van Bussel GJW. Wind turbine fatigue loads as a function of atmospheric conditions offshore. Wind Energy Oct 2016;19(10):1917–32. 1099-1824. https://doi.org/10.1002/WE.1959. https://onlinelibrary.wiley.com/doi/full/10.1002/we.1959.

[56] Shinozuka M, Jan. C-M. Digital simulation of random processes and its applications. J Sound Vib Nov 1972;25(1):111–28. 0022-460X. https://doi.org/10.1016/0022-460X(72)90600-1. https://ui.adsabs.harvard.edu/abs/1972JSV....25..111S/abstract.

[57] Cheynet E. WindSimFaster; 2024. https://nl.mathworks.com/matlabcentral/fileexchange/163676-windsimfaster-windsimfast-but-faster.

[58] Wang J, Cheynet E, ór Snæbjörnsson J, Bogunović Jakobsen J. Coupled aerodynamic and hydrodynamic response of a long span bridge suspended from floating towers. J Wind Eng Ind Aerodyn 2018;177:19–31. 0167-6105. https://doi.org/10.1016/j.jweia.2018.03.024. https://www.sciencedirect.com/science/article/pii/S0167610517309108.

[59] Shinozuka M, Deodatis G. Simulation of stochastic processes by spectral representation. Appl Mech Rev Apr 1991;44(4):191–204. 0003-6900. https://doi.org/10.1115/1.3119501

[60] Dangi N, Sodja J, Wei Y. Divergence-free correction for synthetic wind fields. Wind Energy 2025;28(11):e70062. https://doi.org/10.1002/we.70062

[61] Veers PS. Three-dimensional wind simulation. English. Tech. rep. United States 1988. https://www.osti.gov/biblio/7102613.

[62] Cheynet E. Wind-induced vibrations of a suspension bridge: a case study in full-scale. In: *PhD thesis University of Stavanger* (Dec 2016). 1890-1387. https://uis.brage.unit.no/uis-xmlui/handle/11250/2425472.

[63] Lenschow DH, Stankov BB. Length scales in the convective boundary layer. Journal of Atmospheric Sciences 1986;43(12):1198–209.

[64] Robertson AN, Shaler K, Sethuraman L, Jonkman J. Sensitivity analysis of the effect of wind characteristics and turbine properties on wind turbine loads. Wind Energy Sci Sept 2019;4(3):479–513. 23667451. https://doi.org/10.5194/WES-4-479-2019

[65] Rivera-Arreba I, Wise AS, Eliassen LV, Bachynski-Polić EE. Effect of atmospheric stability on the dynamic wake meandering model applied to two 12MW floating wind turbines. Wind Energy 2023;26(12):1235–53. https://doi.org/10.1002/we.2867

[66] Shaler K, Jonkman J, Doubrawa P, Hamilton N. FAST.Farm response to varying wind inflow techniques: preprint. Tech. rep. NREL/CP-5000-72893, Jan 2019. https://www.nrel.gov/docs/fy19osti/72893.pdf.

[67] Wise A, Bachynski EE. Analysis of wake effects on global responses for a floating two-turbine case. J Phys Conf Ser Oct 2019;1356(1):12004. https://doi.org/10.1088/1742-6596/1356/1/012004

[68] Wise AS, Bachynski EE. Wake meandering effects on floating wind turbines. Wind Energy 2020;23(5):1266–85. https://doi.org/10.1002/we.2485

[69] Jonkman J, Sprague M, et al. OpenFAST — wind research — NREL; 2022. https://www.nrel.gov/wind/nwtc/openfast.html.

[70] Guntur S, Jonkman J, Sievers R, Sprague MA, Schreck S, Wang Q. A validation and code-to-code verification of FAST for a megawatt-scale wind turbine with aeroelastically tailored blades. Wind Energy Sci Jul 2017;2(2):443–68. 23667451. https://doi.org/10.5194/WES-2-443-2017

[71] David JL, Hansen AC, Jeff EM. Validation of the AeroDyn subroutines using NREL unsteady aerodynamics experiment data. Wind Energy 5.2–3 Apr 2002, pp. 227–44. 1099-1824. https://doi.org/10.1002/WE.69. https://onlinelibrary.wiley.com/doi/full/10.1002/we.69%20https://onlinelibrary.wiley.com/doi/abs/10.1002/we.69%20https://onlinelibrary.wiley.com/doi/10.1002/we.69.

[72] Boorsma K, Schepers G, Madsen HA, Pirrung G, Sørensen N, Bangga G, Imiela M, Grinderslev C, Forsting AM, Shen WZ, Croce A, Cacciola S, Schaffarczyk AP, Lobo B, Blondel F, Gilbert P, Boisard R, Höning L, Greco L, Testa C, Branlard E, Jonkman J, Vijayakumar G. Progress in the validation of rotor aerodynamic codes using field data. Wind Energy Sci Feb 2023;8(2):211–30. 2366-7443. https://doi.org/10.5194/WES-8-211-2023. https://wes.copernicus.org/articles/8/211/2023/.

[73] Carmo L, Bergua R, Wang L, Robertson A. Validation of local structural loads computed by OpenFAST against measurements from the FOCAL experimental campaign. In: Proceedings of the international conference on offshore mechanics and arctic engineering - OMAE, vol. 7; Aug 2024. https://doi.org/10.1115/OMAE2024-128114

[74] NREL. ROSCO toolbox. *GitHub repository* (2021. https://github.com/NREL/ROSCO.

[75] Meklenborg Miltersen Slot R, Svenningsen L, Sørensen JD, Thøgersen ML. Consistent direct-drive version of the NREL 5MW turbine. Tech. rep Aalborg, Denmark: Allborg University; 2018. https://vbn.aau.dk/en/publications/consistent-direct-drive-version-of-the-nrel-5mw-turbine/.

[76] Hendriks HB, Bulder BH. Fatigue equivalent load cycle method. Tech. rep. Petten: Energy Research Centre of the Netherlands (ECN), Apr 1995. https://publicaties.ecn.nl/PdfFetch.aspx?nr=ECN-C%E2%80%9395-074.

[77] Thomsen K. The statistical variation of wind turbine fatigue loads. In: IEA joint action. Wind turbine fatigue. Technical University of Denmark. Department of Fluid Mechanics, Oct 2000. p. 1–15. https://orbit.dtu.dk/en/publications/the-statistical-variation-of-wind-turbine-fatigue-loads-2.

[78] Ahmadi MHB, Yang Z. On wind turbine power fluctuations induced by large-scale motions. Appl Energy 2021;293:116945. 0306-2619. https://doi.org/10.1016/j.apenergy.2021.116945. https://www.sciencedirect.com/science/article/pii/S0306261921004220.

[79] Chamorro LP, Hill C, Neary VS, Gunawan B, Arndt REA, Sotiropoulos F. Effects of energetic coherent motions on the power and wake of an axial-flow turbine. Phys Fluids 2015;27.5. https://doi.org/10.1063/1.4921264. https://www.scopus.com/inward/record.uri?eid=2-s2.0-84930225627&doi=10.1063%2f1.4921264&partnerID=40&md5=7213280dce0104008aa449a2937da686.

[80] Ahmadi MHB, Yang Z. Numerical study of the coupling between the instantaneous blade loading/power of an axial wind turbine and upstream turbulence at high reynolds numbers. Energy 2020;207:118167. 0360-5442. https://doi.org/10.1016/j.energy.2020.118167. https://www.sciencedirect.com/science/article/pii/S0360544220312743.

[81] Payne GS, Stallard T, Martinez R, Bruce T. Variation of loads on a three-bladed horizontal axis tidal turbine with frequency and blade position. J Fluids Struct 2018;83:156–70. 0889-9746. https://doi.org/10.1016/j.jfluidstructs.2018.08.010. https://www.sciencedirect.com/science/article/pii/S0889974617306734.

[82] Howard KB, Hu JS, Chamorro LP, Guala M. Characterizing the response of a wind turbine model under complex inflow conditions. Wind Energy 2015;18(4):729–43. https://doi.org/10.1002/we.1724

[83] Dangi N. NWO grant computing time. Amsterdam: the Dutch research council (NWO). Tech. rep. Sept 2025. https://doi.org/10.61686/PYGAY28487

[84] Delft High Performance Computing Centre (DHPC). DelftBlue supercomputer (phase 2); 2024. https://www.tudelft.nl/dhpc/ark:/44463/DelftBluePhase2.